

Femtosecond Laser-Induced Crystallization in Glasses: Growth Dynamics for Orientable Nanostructure and Nanocrystallization

Jing Cao, Matthieu Lancry, Francois Brisset, Leo Mazerolles, Romuald Saint-Martin, Bertrand Poumellec

▶ **To cite this version:**

Jing Cao, Matthieu Lancry, Francois Brisset, Leo Mazerolles, Romuald Saint-Martin, et al.. Femtosecond Laser-Induced Crystallization in Glasses: Growth Dynamics for Orientable Nanostructure and Nanocrystallization. Crystal Growth & Design, 2019, 19 (4), pp.2189-2205. 10.1021/acs.cgd.8b01802 . hal-02367880

HAL Id: hal-02367880
https://hal.science/hal-02367880

Submitted on 7 Nov 2021

HAL is a multi-disciplinary open access archive for the deposit and dissemination of scientific research documents, whether they are published or not. The documents may come from teaching and research institutions in France or abroad, or from public or private research centers.

L'archive ouverte pluridisciplinaire **HAL**, est destinée au dépôt et à la diffusion de documents scientifiques de niveau recherche, publiés ou non, émanant des établissements d'enseignement et de recherche français ou étrangers, des laboratoires publics ou privés.

Femtosecond laser-induced crystallization in glasses: growth dynamics for orientable nanostructure and nano crystallization

Jing Cao[†], *Matthieu Lancry*[§], *François Brisset*[§], *Léo Mazerolles*[⊥], *Romuald Saint-Martin*[§], *and Bertrand Poumellec*[§*]

[†]College of Chemistry and Molecular Engineering, Peking University, 100871, Beijing, P. R. China

[§]Synthèse, Propriété et Modélisation des Matériaux in Institut de Chimie Moléculaire et des Matériaux d'Orsay (ICMMO), UMR CNRS-UPSud 8182, Université Paris Sud in Université Paris Saclay, Bâtiment 410, 91405 Orsay Cedex, France

[⊥]Institut de Chimie et des Matériaux Paris-Est, Université Paris Est, CNRS UMR 7182, 2-8 rue Henri Dunant, 94407 Thiais, France

ABSTRACT: Laser-induced crystallization in glasses is of great interest because of its significant applications in optics. However, the mechanisms involved are not yet concluded and this paper is to make progress on this problem. Major aspects of the laser-induced crystallization are the nanostructure formation, textured crystallization, and growth dynamics. Herein, firstly, we review the previous works on the laser-induced crystallization in various glasses by different kinds of lasers. Then lithium niobium silicate glasses were used as a "glass model" to investigate the nanostructure formation and crystallization by fs laser irradiation at high repetition rate (100-500 kHz). Based on the deposited fs laser power inside glasses, three crystallization regimes can be classified with the increase of laser power. In addition, the boundary between neighboring regimes can be adjusted by changing the writing parameters (e.g. focus depth). Regime 1: modifications of the amorphous structure. Regime 2: phase separation into crystalline $LiNbO_3$ and amorphous SiO_2. There is appearance of an organized lamellar nanostructure and textured nanocrystals, embedded in amorphous lamellas. Polar axes are perpendicular to laser polarization direction. Remarkably, this hierarchical micro/nanostructure can induce an orientation tunable second harmonic generation and form birefringence. Regime 3: crystallization morphology is sensitive to the angle between laser writing and laser polarization direction. With parallel configuration, crystal grains are at the micron scale. With perpendicular configuration, crystal morphologies resemble regime 2 but they are not textured. In this paper, a crystallization dynamic model is proposed to explain the nano/micro-crystals formation and their morphology induced by fs laser irradiation. This model allows thinking that it is very likely possible to extend conclusions to other non-congruent glasses. This provides guidelines for manufacturing a wide variety of multifunctional optical devices.

1. INTRODUCTION

For the last decades, laser-induced crystallization in glasses has received widely attention because of its potential applications in photonics [1, 2]. From the technical perspective, laser-induced crystallization in glasses is an effective approach for fabricating transparent matter with designed shapes/nanostructures [3]. Meanwhile, it is a clean, precise, non-contact, and flexible method with various parameters to adjust in comparison with heat treatment [4, 5]. From the scientific point, it is an important topic for understanding the phase transformation behavior in laser-irradiated glasses [6-9]. Generally, after the precipitation of crystalline phases, enhanced properties (e.g. strength and toughness) and/or new functionalities (second order non-linear optical properties [10], linear or circular optical anisotropies) can be obtained in comparison to the parent glasses [5, 9, 11, 12].

In this paper, firstly we review the types of lasers used and related mechanism for obtaining crystal in glasses, with a strong focus on optically nonlinear crystalline phase formation. Then, as a model, we summarize the recent progress in lithium niobium silicate (LNS) glasses. Crystalline texture and nanostructure are dependent on the laser parameters (e.g. pulse energy, repetition rate, speed of scanning, laser polarization). What is remarkable is that texture and nanostructure orientation can be adjusted according to the laser polarization direction for some range of the laser parameters. From this, resulting optical properties can be also oriented like: second harmonic generation (SHG) and form birefringence. Some cases for controlling the crystal orientation have been listed. Finally a crystallization mechanism, especially the growth dynamics in the case of the fs laser-induced crystallization in glasses is proposed. For comparison, crystallization using the well-known floating-zone method has been also performed.

1.1 Laser types

It has been demonstrated by Komatsu et al. [9, 13], Hirao et al. [14], Miura et al. [15], Honma et al. [16], Qiu et al. [2, 17], Jain et al. [18], Sigaev et al. [19, 20], and Poumellec et al. [21] that it is possible to induce crystallization in glasses with various lasers, such as continuous wave (CW) laser [22], long laser pulses (e.g. ns laser [19]), and ultra-short laser pulses (e.g. fs laser [5, 23]). The first steps of interaction of each laser with glasses are described in the next paragraph.

CW lasers

Wide-band gap materials (e.g. most oxide glasses) are transparent in the visible to near infrared regime (ca. 400-1700 nm) at low-intensity light radiation, because the incident photon energy is smaller than material band gap energy. The linear light absorption is thus weak. Thus the heat effect induced by most CW lasers (e.g. Nd:YAG laser, 1064 nm) working in the visible/ near infrared regime is too weak to initialize glass crystallization. However, crystals can appear in glass by introducing transition metal ions (e.g. Fe^{2+} with small amount, i.e. > 1 mol%) or rare-earth ions (e.g. Dy^{3+} with larger amount, i.e. > 8 mol%), i.e., transition metal atom heat processing or rare-earth atom heat processing [24, 25]. In this case, the CW laser energy (e.g. Nd:YAG laser, 1064 nm) can be absorbed linearly through the doping ions and then transferred to the glass matrix by non-radiative relaxation process (electron-phonon coupling) [13]. The surrounding of the doping ions is heated and if the temperature of the laser-irradiated region is high enough, structural modifications (e.g. crystallization) occur in the focal point region [26]. However, as the glass absorbs linearly the incident laser, the crystallization is limited at the glass surface.

The laser parameters (e.g. laser power) or chemical compositions play an important part in the formed structural geometry. Komatsu et al. [24] shown that for $10Sm_2O_3$-$35Bi_2O_3$-$55B_2O_3$ glass,

CW Nd:YAG laser (1064 nm), a homogeneous crystal line (width of ~5 μm) was obtained at 0.66 W, but when laser power is larger than 0.8 W, crystal lines with a rough morphology occur.

CW laser (e.g. CO_2 laser 10.6 μm, ~1.7 W) can induce crystallites in glass (e.g. $11TiO_2$-$63BaO$-$26B_2O_3$, wt%) showing the same morphology as the ones crystallized by conventional thermal treatment. However, the crystal growth rate appears higher than the one obtained from an electric furnace [27]. Using the heat-assisted Ti-Sapphire CW laser (800 nm), polycrystalline lines and dots can be produced in $Nd_{0.2}La_{0.8}BGeO_5$ glass and the crystallization occurs congruently similarly to the one of devitrification through furnace heating [28]. However, for (100-x)$LiBO_2$-xNb_2O_5 ($5 \leq x \leq 20$) glasses, after the heat treatment and then being exposed to laser irradiation (1064 nm), $LiBO_2$ or $Li_2B_4O_7$ phases are formed when $x \geq 5$; whereas $LiNb_3O_8$ phase formation appears with the increase of Nb_2O_5 ($x \geq 20$) [29]. Note that the initial crystalline phase can be decomposed for long laser irradiation time (e.g. CW YAG laser, 1W, 1064 nm, 10 BaO-$10Sm_2O_3$-$80TeO_2$ at 60 s) [22].

Table 1 displays the CW laser crystallization of commonly used glasses. Sometimes, the glass is heated during the laser irradiation because it was difficult to induce crystallization by the laser solely without this process [30]. The external sample heating decreases the cooling rate of the laser-irradiated zones, helping in crystallization and preventing crack formation [31]. There is a separated process of heating and laser irradiation. For example, $10Sm_2O_3$-$40BaO$-$50B_2O_3$ glass was heated at ~150°C to avoid the fracture of glasses; crystal grains (on the glass surface) with a diameter of 5~30 μm were prepared by a sintering method. Then the crystal grains on the surface were irradiated by a CW Nd:YAG laser and these grains were dissolved inside the glasses, thus forming crystalline dots [16].

Table 1. Glass compositions and the formed nonlinear optical crystalline phases by CW laser irradiation

Glass composition (mol%)	Crystalline phase	Irradiation conditions	Refs
$15K_2O$-$15Sm_2O_3$-$70P_2O_5$	$KSm(PO_3)_4$	heat-assisted CW Nd:YAG laser, 1064 nm, 0.8 W	[32]
$10BaO$-xLn_2O_3-$(10-x)Sm_2O_3$-$80TeO_2$ (Ln: La, Er)	$Sm_2Te_6O_{15}$	CW Nd:YAG laser, 1064 nm, 0.5-0.7 W	[33]
$10RO$-$10Sm_2O_3$-$80TeO_2$ (R: Mg, Ba)	$Sm_2Te_6O_{15}$	CW YAG laser, 1064 nm, 1 W, 30-60 s	[22]
$10Sm_2O_3$-10SrO-10BaO-$20Nb_2O_5$-$50B_2O_3$ or $8Sm_2O_3$-10SrO-10BaO-$20Nb_2O_5$-$52B_2O_3$	Sm^{3+}-doped $Sr_xBa_{1-x}Nb_2O_6$	heat-assisted CW Nd:YAG laser, 1064 nm, 1 W	[30]
$22.5RE_2O_3$-$47.5MoO_3$-30 B_2O_3 (RE: Sm, Gd, Tb, and Dy)	β'-$RE_2(MoO_4)_3$	CW Yb:YVO_4 fiber laser, 1080 nm, 0.5-2.0 W, 8-20 μm/s	[34]
$21.25Sm_2O_3$-$63.75MoO_3$-$15B_2O_3$	β'-$Sm_2(MoO_4)_3$	CW Nd:YAG laser, 1064 nm, 0.4 W	[35]
$8Sm_2O_3$-$37Bi_2O_3$-$55B_2O_3$	$Sm_xBi_{1-x}BO_3$	CW Nd:YAG laser, 1064 nm, ~0.9 W	[26]
$10Sm_2O_3$-$35Bi_2O_3$-$55B_2O_3$	$Sm_xBi_{1-x}BO_3$	CW Nd:YAG laser, 1064 nm, 0.66 W	[24]
$10Sm_2O_3$-40BaO-$50B_2O_3$	β-BaB_2O_4	heat-assisted CW Nd:YAG laser, 1064 nm, 0.6 W	[16]
$10Dy_2O_3$-45BaO-$45B_2O_3$	β-BaB_2O_4	heat-assisted CW Nd:YAG laser, 1064 nm, 0.9 W	[16]
$11TiO_2$-63BaO-$26B_2O_3$ (wt%)	β-BaB_2O_4	CO_2 laser 10.6 μm, ~1.7 W	[27]
2NiO-$1.1Y_2O_3$-29.8BaO-$33.1Nb_2O_5$-$36B_2O_3$	$Ba_{1-x}Y_{2x/3}Nb_2O_6$	CW Yb:YVO_4 fiber laser, 1080 nm, 1.9 W, 4 μm/s	[36]
2NiO-$4La_2O_3$-16SrO-16BaO-$32Nb_2O_5$-$30B_2O_3$	$Sr_{0.5}Ba_{0.5}Nb_2O_6$	by heat-assisted CW Nd:YAG laser 1064 nm, 1W, 1 μm/s	[37]
$Sm_{0.5}La_{0.5}BGeO_5$☼	$LaBGeO_5$	heat-assisted Nd:YAG CW laser,	[31]

		1064 nm, 0.98 W, 1 μm/s	
$Nd_{0.2}La_{0.8}BGeO_5$	$LaBGeO_5$	heat-assisted Ti-Sapphire CW laser, 800 nm, 1.1 W	[28]
NiO-, Fe_2O_3-, and V_2O_5-doped (0.3-1%) 33.3BaO-16.7TiO_2-50GeO_2	$Ba_2TiGe_2O_8$	CW Nd:YAG laser, 1064 nm, 1.0 W	[25]
CuO (1%)-doped 25Li_2O-25Nb_2O_5-50TeO_2	$LiNbO_3$	heat-assisted CW Nd:YAG laser, 1064 nm, 0.59 W	[38]
0.5CuO-35Li_2O-30Nb_2O_5-35SiO_2	$LiNbO_3$	CW Yb-fiber laser laser, 1080 nm, 1.3 W	[39]
0.5CuO-40Li_2O-32Nb_2O_5-28SiO_2	$LiNbO_3$	CW Yb-fiber laser laser, 1080 nm, 1.3 W	[39]
5Sm_2O_3-35Li_2O-30Nb_2O_5-20SiO_2-15B_2O_3	$LiNbO_3$	CW Yb-fiber laser laser, 1080 nm, 2.4 W	[39]

Nanosecond lasers

When pulsed lasers are used with a low pulse intensity, the light absorption remains in the linear domain and the requirements for crystallization are the same as for CW lasers: doping is necessary. Sigaev et al. [19] reported the formation of $LaBGeO_5$ in 25La_2O_3-25B_2O_3-50GeO_2 bulk glass with a copper vapor ns laser (510.6 and 578.2 nm, 10-25 ns, 0.1-1.0 mJ, and 10-18 kHz). Like the CW laser case, coloring impurity (i.e. Cr_2O_3) was added to the glass as an absorber to maximize the heat effect for crystallization.

Femtosecond laser specificities

In comparison with the CW lasers or ns laser, the light intensity of a focused fs laser may be as high as several TW/cm^2. In these conditions, fs laser can induce multi-photon ionization or/and tunnelling ionization, leading to electron excitation across the band gap of the material [40,

[41]. Then, energy of the electron may be released partially to the lattice and heat it. This technique allows obtaining the modifications in the transparent glass without adding absorber ions. As the absorption is strongly non-linear, it occurs only in the focal volume (a few tens μm^3) that can be deep inside the glass. The fs laser-induced crystallization may be thus space-selective [5] in three dimensions (3D), instead of affecting only the surface like the CW ones. However, an important condition has to be fulfilled, the repetition rate (ca.> 100 kHz) has to be such that the time between successive laser pulses was shorter than the one for heat to diffuse away from the focal volume (ca. μs scale). In this condition, thermal accumulation in the focal volume occurs and the evolution of the average temperature can be controlled in the course of the writing step. In that case, the required thermal conditions can be fulfilled for crystallization in some places and nucleation and crystal growth can occur. For example, at fixed repetition rate (i.e. 370 fs, 1030 nm, 500 kHz), ZnO crystals can be obtained inside glass above certain average power (i.e. 1000 mW, focal depth 100 μm, irradiation duration 2 minutes) [42].

Stone et al. [43] compared the formation of $LaBGeO_5$ in glass by fs and CW lasers and demonstrated that the formed phases were comparable to CW laser crystallization of Sm-doped glass. But they found notable differences in the line structure and crystal growth rates: fs laser crystallization needs much higher writing speed (20 to 45 μm/s for fs laser and 1 μm/s for CW laser).

Table 2 lists the precipitation of nonlinear optical crystal inside glasses by fs laser irradiation. It is worth noting that, compared with the crystallization obtained by CW laser or ns laser irradiation, based on thermal effect, we demonstrated an effect coming from the characteristics of the fs laser itself (laser polarization effect) in controlling crystallization. We found laser-polarization orientable textured nano crystals [3, 10].

Table 2. Glass compositions and the formed nonlinear optical crystalline phases by fs laser irradiation

Glass composition (mol%)	Crystalline phase	Irradiation conditions	Refs
$47.5BaO\text{-}5.0Al_2O_3\text{-}47.5B_2O_3$	$\beta\text{-}BaB_2O_4$ (BBO)	800 nm, 130 fs, 200 kHz, 600 mW	[23]
$25La_2O_3\text{-}25B_2O_3\text{-}50GeO_2$	$LaBGeO_5$	heat-assisted laser irradiation, 800 nm, 70 fs, 250 kHz, 300 mW, 20 μm/s	[44]
$33.3BaO\text{-}16.7TiO_2\text{-}50SiO_2$	$Ba_2TiSi_2O_8$	800 nm, 150 fs, 250 kHz, 600 mW	[45]
$33.3BaO\text{-}16.7TiO_2\text{-}50SiO_2\text{-}0.05Ag_2O$	$Ba_2TiSi_2O_8$	800 nm, 150 fs, 250 kHz, 600-900 mW	[46]
$33.3BaO\text{-}16.7TiO_2\text{-}50SiO_2$	$Ba_2TiSi_2O_8$	800 nm, 150 fs, 250 kHz, 700-900 mW	[46]
$33.3BaO\text{-}16.7TiO_2\text{-}50SiO_2\text{-}0.5Er_2O_3$	$Ba_2TiSi_2O_8$	800 nm, 150 fs, 250 kHz, 750-950 mW	[17]
$40SrO\text{-}20TiO_2\text{-}40SiO_2$	$Sr_2TiSi_2O_8$	800 nm, 150 fs, 250 kHz, 100-400 mW for dots, 850 mW, 100 μm/s for lines	[47]
$33.3SrO\text{-}16.7TiO_2\text{-}50SiO_2$	$Sr_2TiSi_2O_8$	1030 nm, 300 fs, 300 kHz, 1.7 μJ, 10 μm/s	[48]
$32.5Li_2O\text{-}27.5Nb_2O_5\text{-}40.0SiO_2$	$LiNbO_3$	800 nm, ~120 fs, 200 kHz, ~600 mW	[49]
$30.0Li_2O\text{-}10.0Nb_2O_5\text{-}40.0SiO_2$	$LiNbO_3$	800 nm, ~120 fs, 200 kHz, ~600 mW	[49]
$32.5Li_2O\text{-}27.5Nb_2O_5\text{-}40.0SiO_2$	$LiNbO_3$	1030 nm, 300 fs, 250 kHz, 0.8 μJ/pulse, 5 μm/s	[10]
$33Li_2O\text{-}33Nb_2O_5\text{-}34SiO_2$	$LiNbO_3$	1030 nm, 300 fs, 300 kHz, 0.5-2.2μJ/pulse, 5 μm/s	[3]
$33Li_2O\text{-}33Nb_2O_5\text{-}34SiO_2$	$LiNbO_3$	1030 nm, 300 fs, 500 kHz, 0.8-2.2 μJ/pulse, 5 μm/s	[21]

Glass chemical composition may have an effect on the choice of fabrication parameters [33]. For $5.0Na_2O$-$36.0BaO$-$39.0TiO_2$-$20.0SiO_2$ glass, the irradiation time of laser (800 nm, ~120 fs, 200 kHz) needed for the crystallization can be drastically decreases from a few minutes to 1 s or so by adding Na_2O to the ternary system [49]. Zhu et al. [46] demonstrated that crystal precipitation can be largely enhanced by doping BaO-TiO_2-SiO_2 glass with Ag^+-doped (800 nm, 250 kHz, and 150 fs). Honma et al. [50] demonstrated that for $10Sm_2O_3$-$40BaO$-$50B_2O_3$ glass, no suitable laser irradiation conditions can be found for obtaining β-BaB_2O_4 (β-BBO) crystal curved lines. It takes shorter time for crystal formation in $32.5Li_2O$-$27.5Nb_2O_5$-$40.0SiO_2$ glass than that of $30.0Li_2O$-$10.0Nb_2O_5$-$40.0SiO_2$ one (800 nm, ~120 fs, 200 kHz, ~600 mW) [49]. On the contrary, for $10Sm_2O_3$-$42BaO$-$48B_2O_3$ glass, crystal curved line can be obtained (0.63 W, 7 μm/s). But when increasing the writing speed to 10 μm/s, no β-BBO crystal curved lines were recorded. So, the laser-induced crystallization in glass is multi-parameters dependent, which is better to give the fabrication information in full details.

1.2 Results in lithium niobium silicate (LNS) glasses with fs laser

Recently, our group [3] demonstrated that the high repetition rate fs laser (e.g. 300 fs, 300 kHz) induced crystallization in glass is far beyond to be only a thermal effect. Three regimes are found according to the pulse energy in LNS glass (illustrated in

Figure 1). For regime 1, the low pulse energy, no crystal was obtained but with a modification of the amorphous phase was observed, with a faster chemical etching rate than the glass matrix (i.e zone B in **Figure 1**a). At moderate pulse energy (i.e. regime 2, e.g. 0.5-0.9 μJ/pulse, 300 kHz), textured nanocrystals (i.e zone C in **Figure 1**b) can be obtained with polar axis distributed perpendicular to the writing laser polarization direction [10]. If we continue to increase the pulse energy (i.e. regime 3 of LNS glass), two kinds of crystalline zones are obtained: the center rough

crystal zone (i.e zone D in **Figure 1**c and **Figure 1**d) and the surrounding outside smooth crystal part (i.e zone D in **Figure 1**c and **Figure 1**d). In addition, the formation of crystal is complex related to writing configuration (the relationship between the writing and laser polarization directions) [3]. Interestingly, nanoscale phase separation was obtained in regime 2 and regime 3: $LiNbO_3$ nonlinear crystals embedded in lamella-like frames of amorphous SiO_2. These amorphous frames orientation are polarization-controllable, which are oriented perpendicular to laser polarization direction. Furthermore, this self-assembly nanostructure, containing textured nanocrystals, can induce a form birefringence quite differently from the one appearing in silica glass [51].

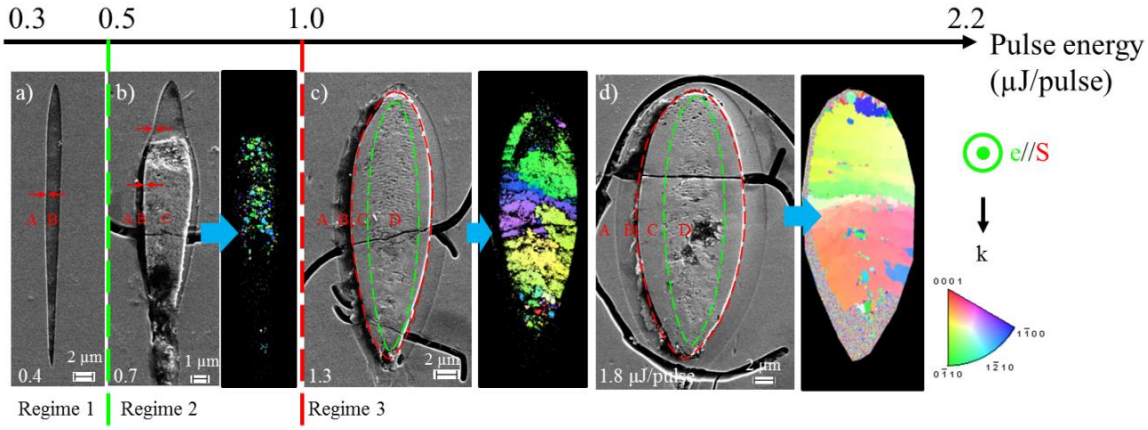


Figure 1. High repetition rate fs laser-induced three regimes in lithium niobium silicate (LNS) glass according to pulse energy (indicated in the left bottom of each picture in white). The left image is SEM and the right image is the according EBSD map of the cross section of the irradiated line (i.e. the scanning direction is perpendicular to the paper plane). The color in EBSD map is based on $LiNbO_3$ space group (i.e. R3c), coding along laser polarization direction. Laser polarization direction is marked by green e. The scanning direction is displayed by S. The laser came from the top (illustrated by k). Other parameters: $33Li_2O$-$33Nb_2O_5$-$34SiO_2$ (mol%), 1030 nm, 300 fs, 300 kHz, 5 μm/s, and focus depth 350 μm. The picture is modified based on [3, 7, 51].

1.3 Crystal orientation can be sometimes controlled

Table 3. Crystal orientation observed in some experiments

Laser parameters	Glass composition (mol%)	Crystal	Crystal orientation	Refs

Heat-assisted CW Nd:YAG 1064 nm, 1 W, 1 μm/s	$2NiO\text{-}4La_2O_3\text{-}16SrO\text{-}16BaO\text{-}32Nb_2O_5\text{-}30B_2O_3$	$Sr_{0.5}Ba_{0.5}Nb_2O_6$	c-axis orientations in the direction of scanning	37
Heat-assisted CW Nd:YAG 1064 nm, 0.9 W, 3-8 μm/s	$10Dy_2O_3\text{-}45BaO\text{-}45B_2O_3$	β-BBO	idem	16
CW Yb:YVO_4 1080 nm, 0.8 W, and 4 μm/s	$8Sm_2O_3\text{-}42BaO\text{-}50B_2O_3$	β-BBO	Idem even with bending and curved shaped (bending angle<60 ˚)	52
CW Yb:YVO_4 1080 nm, 1.9 W, 4 mm/s, 20 mm beneath the surface	$64Ba_{1-x}Y_{2x/3}Nb_2O_6\text{-}36B_2O_3$	$Ba_{1-x}Y_{2x/3}Nb_2O_6$ nanocrystals	idem	36
Heat-assisted fs laser 800 nm, 130 fs, 250 kHz, 300 mW, 42 μm/s	$25La_2O_3\text{–}25B_2O_3\text{–}50GeO_2$	$LaBGeO_5$	idem	14
Heat-assisted fs laser 800 nm, 70 fs, 250 kHz, 300 mW, 20 μm/s	$20La_2O_3\text{–}40H_3BO_3\text{–}40GeO$	$LaBGeO_5$	idem even after bending	44

Inspecting the **Table 3** where are reported several experiments, we could deduce that for different types of lasers, the c-axis is always observed oriented, along the scanning direction. But interestingly, our group showed that, just by adjusting the writing laser polarization direction during a fs laser irradiation at moderate pulse energies, the c-axis of nano-sized $LiNbO_3$ can be adjusted (e.g. 1030 nm, 300 fs, 300 kHz, 0.5-0.9 μJ/pulse, illustrated in **Figure 1**b). In contrast at quite large energies (e.g. 1030 nm, 300 fs, 300 kHz, 1.0-2.2 μJ/pulse, displayed in **Figure 1**c and **Figure 1**d), other textures occur, where the crystal orientation is variable along laser propagation direction or scanning direction [3]. Recently, Veenhuizen et al. [53] shown that if the energy is large enough (1026 nm, 175 fs, 200 kHz, 2.6-4.2 μJ/pulse, heated at 500 ˚C) there is only one grain in the direction of scanning.

So far, the formation mechanism of laser-induced crystallization, especially with nanostructure still remains a mystery. This paper is intended to make progress on this problem from the perspectives of crystal orientation control, nanostructure formation, and growth dynamics. LNS glasses were employed as a model due to the merits such as optically transparent, large range composition of forming glass [54], and effective crystallization [49]. In addition, the formed nonlinear optical crystal ($LiNbO_3$) presents remarkable properties including high Curie temperature (approximately 1210 °C) [55] and large nonlinear coefficient (d_{33}=34.4 pm/V) [56].

Herein, we extend the repetition rate from 100 to 500 kHz. Details of the fs laser-induced crystallization with nanostructure were recorded. A combination of scanning electron microscope (SEM), electron backscatter diffraction (EBSD), and transmission electron microscopy (TEM) was used to reveal the fs laser induced modifications inside LNS glasses (e.g. morphology and crystallization). In addition, the linear and non-linear optical properties (e.g. birefringence and second harmonic generation) are also investigated. Finally, the crystal formation dynamics are exposed in details including a critical discussion with respect to the literature.

2. EXPERIMENTAL SECTION

Due to the poor ability of $LiNbO_3$ for glass forming, it is necessary to add glass formers (e.g. SiO_2, B_2O_3, TeO_2, and P_2O_5) [57]. Herein, SiO_2 is chosen as the glass former due to its physical properties and that it has been largely studied. It is desirable that this glass former does not have cations, modifying the $LiNbO_3$ lattice because of silica's small ionic radius and coordination number [57]. In addition, homogeneous and transparent LNS glasses can be fabricated in large range chemical compositions [54]. Here, glasses with composition of $32.5Li_2O$-$27.5Nb_2O_5$-$40SiO_2$

(mol %) and $33Li_2O$-$33Nb_2O_5$-$34SiO_2$ (mol %) were prepared by melt-quenching method [58]. The glass was cut and then finely polished to reach optical quality for the subsequently laser irradiations.

A commercial Yb-doped fiber amplifier fs laser (Satsuma, Amplitude Systèmes Ltd.) was used as irradiation source (1030 nm, 300 fs). As shown in **Figure 2**, glass was placed with surface normal to the laser propagation direction (i.e. k direction or along +Z direction in the Cartesian coordinate system). A linearly polarized beam was focused using an aspheric lens (numerical aperture NA=0.6) inside the glass at a given depth.

Considering that the crystallization at the glass surface is influenced by various factors (e.g. surface quality, scratches, foreign particles, and cracks [59]), commonly it is hard to obtain long and homogeneous crystal lines at the glass surface. In contrast, the inside of glass is basically homogeneous. However, the nucleation occurs more easily at the surface compared with the inside one. Herein, fs laser was focused inside the glasses and at various focus depths to investigate the crystalline behavior of LNS glasses.

Lines were written in the plane perpendicular to the laser propagation direction (i.e. the XY plan, ttransverse writing geometry) at various scanning speeds (from 5 to 25 μm/s). A half-wave plate placed along light path controlled the linear polarization. Here, the direction of writing laser polarization is given in reference to +X in XY plane (illustrated by e in **Figure 2**). The XY plane is defined based on a laboratory reference. More details are given in ref. [60]. The scanning direction is marked by S in **Figure 2**.

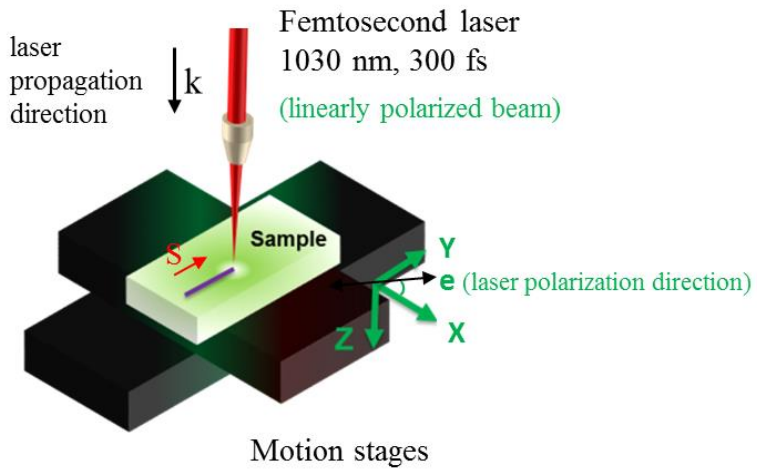


Figure 2. Schematic of fs laser fabrication set-up (k is the laser propagation direction, e illustrated the linearly polarization direction, and S is the scanning direction).

To increase the contrast of scanning electron microscope (SEM) image for the following experiment, the sample was slightly etched with HF (10%, 2 min). Morphology and crystallization of the polished irradiated lines were measured by a field-emission gun scanning electron microscope (FEG-SEM ZEISS SUPRA 55 VP) equipped with EBSD. Image quality (IQ) map constructed from EBSD data provides an effective approach to visualize microstructure [61]. It is a map with a grayscale component according to the relative intensity of the diffraction pattern, generally, with the maximum IQ value in white and the minimum one in black. The contrast in this image may be due to the phase, strain, and grain boundaries. The black parts at of the irradiated area may be due to second phase inclusions (the amorphous one) or grain boundaries, or cracks.

Transmission electron microscopy (TEM) observations were performed on a TOPCON 002B electron microscope operating at 200 keV. The sample was dissected by focused ion beam (FIB) to reduce its thickness down to ~50 nm for TEM observations. Details of the process of FIB treatment are discussed in [7].

The birefringence orientation of irradiated line was determined by a polarized light microscopy (OLYMPUS BX60) with a full-wave retardation plate placed between crossed polarizers.

3. RESULTS

For pulse energy lower than the crystallization threshold (i.e. regime 1 [3]), laser-modified amorphous region can be achieved: with fast HF etch rate than the glass matrix and isotropic negative refractive index change [21]. This has been consistent with a change of fictive temperature. Considering this paper is focused on the laser-induced crystallization, for details of the modified amorphous region's properties, please refer to [21].

3.1 Static mode & scanning mode

A static irradiation was performed before scanning lines inside LNS glass. The static irradiation mode means irradiating the glass without moving the translation stage for a certain time. The static crystallization threshold is defined as the lowest pulse energy to obtain green emission around the focal point of the laser beam at the incident laser irradiation. Green light (at 515nm) was used as a criterion of the nonlinear optical $LiNbO_3$ crystals precipitation inside glass, which is consistent with the double frequency of the incident fs laser with 1030 nm central wavelength [7]. Generally, it takes some time (up to 80 s) of static irradiation, and then the sample translation stage was moved to write crystalline lines at certain writing velocity (e.g. 5 μm/s). If lines are scanned directly without this static irradiation, it is hard to obtain continue or not possible to obtain green light during fs laser fabrication. In the regime 2, crystallization is local (i.e. where there is light) without influence of the neighboring unirradiated volume (solid-solid transformation). SHG light can arise from illuminated volume where nano crystals are. On contrast, this is not the case in regime 3 (the center is melted and crystallization is out of the

beam) but due to light scattering and the large intensity in the beam, SHG from scattered IR light can be easily detected.

At 250 kHz or 500 kHz (focus depth 300 μm in air), the static mode crystallization threshold is around 0.4 μJ/pulse, but the difference is that it takes few seconds for 500 kHz one, but few minutes for 250 kHz one to obtain green light. In other words, it takes less time for higher repetition rate than for lower repetition rates to induced crystalline onset. This indicates the existence of an incubation state which could reveal that some chemical diffusion should take place by cumulative effect.

The threshold for obtaining crystalline line in LNS glass (i.e. scanning mode) for 250 kHz (focus depth 300 μm in air) is around 0.6 μJ/pulse at 5 μm/s, which is larger than the static mode crystallization threshold (i.e. around 0.4 μJ/pulse). It is worth noting that, with the increase of focus depth (e.g. 500 kHz, 650 μm inside glass), the threshold increase to around 0.8 μJ/pulse, which is discussed in details in [21].

3.2 Formation of the self-organized nanostructure

About the chemical composition of the glasses, we used $32.5Li_2O$-$27.5Nb_2O_5$-$40SiO_2$ and $33Li_2O$-$33Nb_2O_5$-$34SiO_2$ [7]. Production of $LiNbO_3$ crystalline phase implies a phase separation and a second phase rich in silica and so likely amorphous. Investigation by TEM pointed out a very tiny self-organized nanostructure that is recalled in **Figure 3** (bright field mode). In this figure, we see white lines corresponding to an amorphous phase and region between these lines that appear uniformly dark for samples irradiated at high energies (illustrated by **Figure 3**c) and less uniform for sample irradiated at lower energies (shown in **Figure 3**a). The dark region were found corresponding to crystallized part (atomic rows are clearly seen in **Figure 3**b and **Figure 3**d). So, nanostructure is achieved even when the phase separation is probably not completed.

The remarkable feature is that nanostructure is regular with a period smaller than the light wavelength, like in pure silica [62-64]. In addition, we found that it is oriented perpendicular to the laser polarization (illustrated by green double arrows). The question is thus: is this nanostructure produced by light or existing without light even if it is influenced by it?

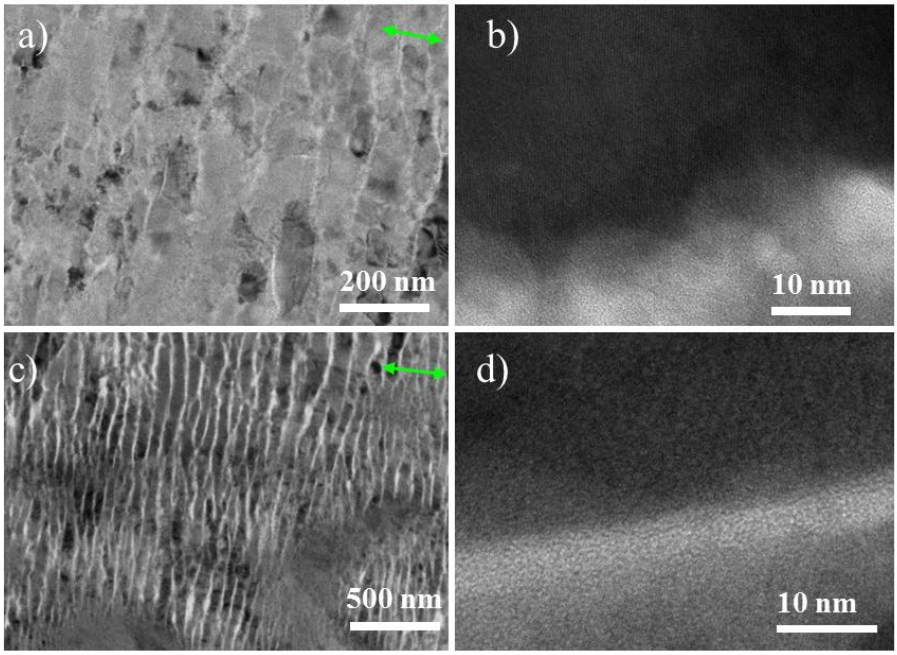


Figure 3. TEM images of the fs laser induced nanostructure in LNS glass at various pulse energies a-b) 0.7 and c-d) 1.3 μJ/pulse (bright field mode). The laser propagation direction is perpendicular to the paper plane. Writing laser polarization direction is indicated by the green double arrows in each image. Other parameters: $33Li_2O$-$33Nb_2O_5$-$34SiO_2$ (mol%), 1030 nm, 300 fs, 300 kHz, 5 μm/s, and focus depth 350 μm.

For understanding this, we investigated the same composition using optical floating-zone method for initiating the phase separation and crystallization. These experiments are reported in Supporting Information. It is interesting to see that an oriented micro-structure was observed after melting. There is self-organisation of the phase separation with a conventional heating method with lines (or lamellas). However, the quasi-period of the structures is much larger than the one observed under fs laser irradiation. There is thus an influence of the light on that phase separation like in pure silica for which stoichiometric oxide separate into solid and gas [65]).

3.3 Rotatable nanostructure orientation of crystallization line (regime 2)

Figure 4a-d display the SEM images of laser-modified zone, formed along the scanning direction, at varying writing laser polarization direction (illustrated by green double arrows in each picture). We can see that nanostructures are formed, oriented perpendicular to the writing laser polarization direction and can be adjusted by rotating it. Moreover, the nanostructure can be preserved along the scanning direction (illustrated by S). Now let us consider **Figure 4**a for detailed discussion. This self-organized nanostructure is clearly visible with alternated white and black parts. The black part (illustrated by red arrows) has a width (d_1) around 56 nm and the white part (marked with green arrows) has a width (d_2) around 104 nm. Even when changing writing laser polarization direction, no big difference of the period has been observed, which is similar to the case in fused silica [66].

It should be mentioned here that the nanostructure has been pointed out in regime 2 or 3 and rotable in both regime. Because of the influence of light, we have to say that the place of the nanostructure indicates the place of irradiating light in regime 2 like in regime 3. This is interesting because from a picture like in **Figure 1**, we can deduce that the light covers the whole modified area in regime 2 but not in regime 3.

Comparing the SEM image (marked by yellow rectangle in **Figure 4**a) and the corresponding EBSD map (**Figure 4**e), we found a quasi-periodic distribution of crystals (i.e. $LiNbO_3$). Due to larger etching rates for SiO_2 than for $LiNbO_3$ [67], the silica rich parts; more chemically etched, appear darker in SEM image. It is worth to note that these nanocrystals are accompanying the nanostructures. For the part without nanostructure, no crystal was detected (illustrated by yellow arrows in **Figure 4**a and **Figure 4**e, regime 2). But, it is also possible to find for low pulse energy, nanostructure without crystallization as we said above [68, 69]. So, probably if the chemical

separation is not achieved largely enough, the crystallization does not occur. We deduce that nanostructure appears before crystallization and this one appears textured as we demonstrated using EBSD.

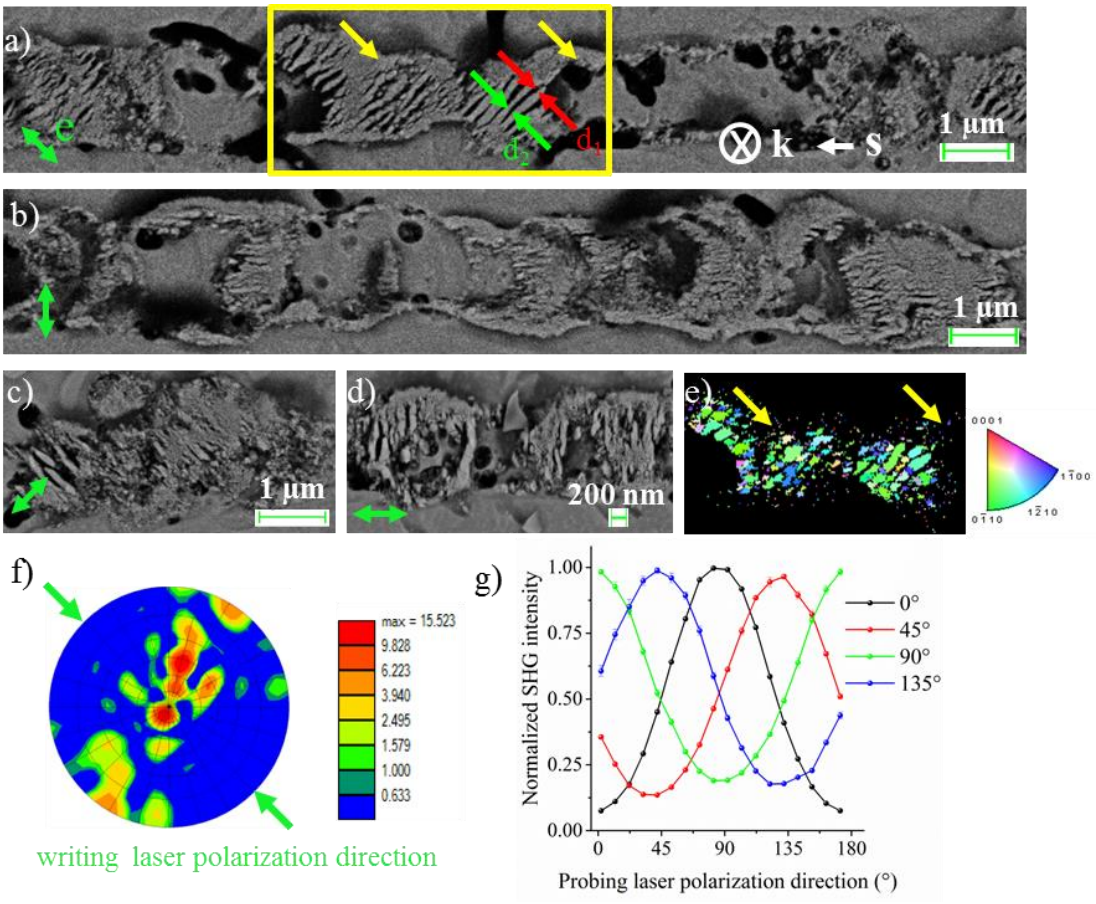


Figure 4. a-d) SEM images of fs laser-induced nanostructures in LNS glass at varying writing laser polarization direction (writing laser polarization direction is indicated by the green double arrows in each image). The corresponding e) IPF image coding in the direction of the laser polarization and f) 0001-PF of the part marked by yellow rectangle in figure a. The color in the EBSD mapping is based on $LiNbO_3$ space group (i.e. R3c), coding along writing laser polarization direction. g) Normalized SHG intensity (normalized at the largest value) as function of probing laser polarization, the variable parameter is writing laser polarization (scanning direction is along 225° [10]), recorded 5 times to obtain average value and standard error. k is the laser propagation direction and S is the scanning direction. Other parameters: $32.5Li_2O$-$27.5Nb_2O_5$-$40SiO_2$ (mol%), 1030 nm, 300 fs, 250 kHz, 0.8 µJ/pulse, 5 µm/s, and focus depth 300 µm in air.

EBSD map displays the position of crystal orientation relative to a sample reference frame. In our case, the colors codes the crystallographic orientation aligned with the considered sample

direction. For example, the red in inverse pole figure (IPF, **Figure 4**e) means crystal <0001> directions are along the coding direction (laser polarization direction). Here, the EBSD map (**Figure 4**e) is totally green or blue but not red, indicating the formation of texture (i.e. preferred orientation). The polar axis (i.e. 0001) is distributed not along writing laser polarization. To have a clear picture of this crystallographic texture, 0001-pole figure (PF) was presented in **Figure 4**f, where the polar axis is distribution along the plane perpendicular to writing laser polarization direction. This is in agreement with previous results obtained at 300 kHz: at the pulse energy slightly higher than crystallization threshold, textured nanocrystal can be obtained [3].

This was the first direct observation of textured nonlinear optical nanocrystals (i.e. $LiNbO_3$) distributed in oriented nanostructures, in which both orientations can be adjusted by rotating writing laser polarization direction. Note that the laser-induced modification is not perfectly homogeneous along the scanning direction, which may due to the inhomogeneity of the glass or instability.

Considering that the second harmonic generation (SHG) is sensitive to the orientation of crystal polar axis [70], the quality of the orientation of crystals in irradiated lines was investigated by normalized SHG intensity as a function of probing polarization [10]. As illustrated in **Figure 4**g, a well-defined cosine-like SHG curve was obtained with maximum shifting with the writing laser polarization orientation. The SHG reaches the maximum value when probing laser polarization is closely perpendicular to writing laser polarization.

We have proposed that for small pulse energies, at the beginning of the crystal growth, the light may produce a laser-induced torques involving the nanocrystal electric dipole [10] (see the following equation) leading to nuclei rotation.

$$\Gamma = DCpart\left(\mathrm{P}_{\omega}^{(1)} \wedge \mathrm{E}_{\omega}^{w}\right) = DCpart\left(\varepsilon_0 \chi^{(1)} \mathrm{E}_{\omega}^{w} \wedge \mathrm{E}_{\omega}^{w}\right)$$

where E_{ω}^{w} is the incident laser electric field and $P_{\omega}^{(1)}$ is the induced dipole at the fs laser frequency during irradiation. $\chi^{(1)}$ is the linear susceptibility.

$LiNbO_3$ is an anisotropic crystal and the largest component of its linear susceptibility is the one perpendicular to the polar axis. This force from the electric field may thus induce the polar axis to be perpendicular to the writing laser polarization. Because the SHG intensity reaches the maximum when probing laser polarization is perpendicular to polar axis, and polar axis of crystal tends to be distributed in the plane perpendicular to writing laser polarization, it can explain why the SHG intensity peaks at the position closely perpendicular to writing laser polarization, and varying with it.

Another proposal could be that a polarization effect on the ferro-electric nuclei freezing the growth when the nucleus polar axis is parallel to the laser polarization. A process a bit similar to the growth of metallic nanoparticles [66, 71]. But we cannot consider that here, as nuclei are not suppressed in this scheme. Just the population of nuclei with c axis perpendicular is enhanced whereas the experiment (like in **Figure 4**f) reveals that there are no crystals with a c-axis parallel to the laser polarization.

Even if the most spectacular effect of the laser polarization influence is for low pulse energy, there is an effect at high pulse energy (regime 3). We recalled at the beginning of the paper that when the pulse energy is high enough and the laser polarization parallel to the scanning direction, the crystallization exhibits large grains including amorphous phase as no chemical migration is detected at the scale of the grains. They are not single crystal, even if EBSD could lead to think the contrary. Veenhuizen et al. [53] showed that for low scanning and high energies, it

is possible to obtain a single texture (only one orientation) on the whole width of the line on several mm. This orientation is such that polar axes of the crystals are all in the direction of scanning. It is worth to note that it is the direction obtained commonly when crystallizing by CW laser (see the beginning of this paper). For CW lasers, no laser polarization is mentioned but for fs laser it is not the case.

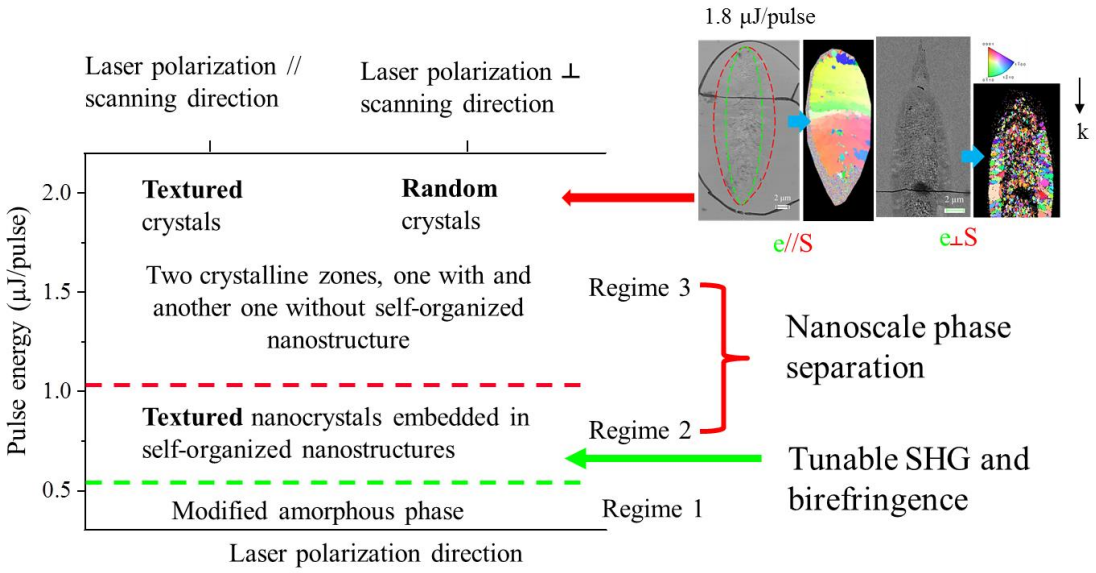


Figure 5. Polarization direction influence according to pulse energy for LNS glasses closed to $30Li_2O$-$30Nb_2O_5$-$40SiO_2$. k is the laser propagation direction, e stands for the writing laser polarization direction, and S is the scanning direction. Other parameters: 1030 nm, 300 fs, NA = 0.6, 300 kHz, 5 µm/s, and focus depth 350 µm.The picture is modified based on [3].

Striking differences are observed when laser polarization is perpendicular to the scanning direction. The grains are much smaller like at small pulse energies, they are also randomly oriented and we point out larger grains neighbouring the edge of modified volume (see **Figure 5** right top). This leads to think that the thermal process is different, which is confirmed by the observation also of a smaller width of the modified area. In the **Figure 5**, we get a decrease from 10 to 6 µm. This is reproducible and just by laser polarization rotation at high pulse energy. This is not observed at low pulse energy.

If the width of the modified area is decreasing, this simply means that the thermal effect is smaller. This leads to think that the absorption of the light energy is smaller. Therefore, either multiphoton absorption coefficient is smaller or the plasma reflectivity is larger. It is difficult to go further without complementary measurements but we point out nevertheless again here an influence of the vector property of light on a thermal process.

3.4 Writing configuration controlled crystallization (Regime 3)

When the pulse energy is increased the pulse energy beyond regime 2, the crystallization becomes complex. In contrast to the ones obtained in regime 2, in which just by changing the writing laser polarization direction, the nanocrystal orientation can be controlled, no matter what the laser scanning direction is, for regime 3, the final crystallization morphology is related to the relative directions of writing and laser polarization.

The SEM image of a line along the scanning direction **Figure 6**a, shows the nanostructure from place to place (magnified image in the red rectangle at the right top) that we discussed above with structures perpendicular to the laser polarization. From their existence, we can delimit the effective width of the light beam, here around 7 μm. It increases with the energy if the depth is the same. As noted before, for that pulse energy (regime 3), the width of the modified area is larger. There is a smooth crystalline region without nanostructure (marked by the blue arrows in **Figure 6**a).

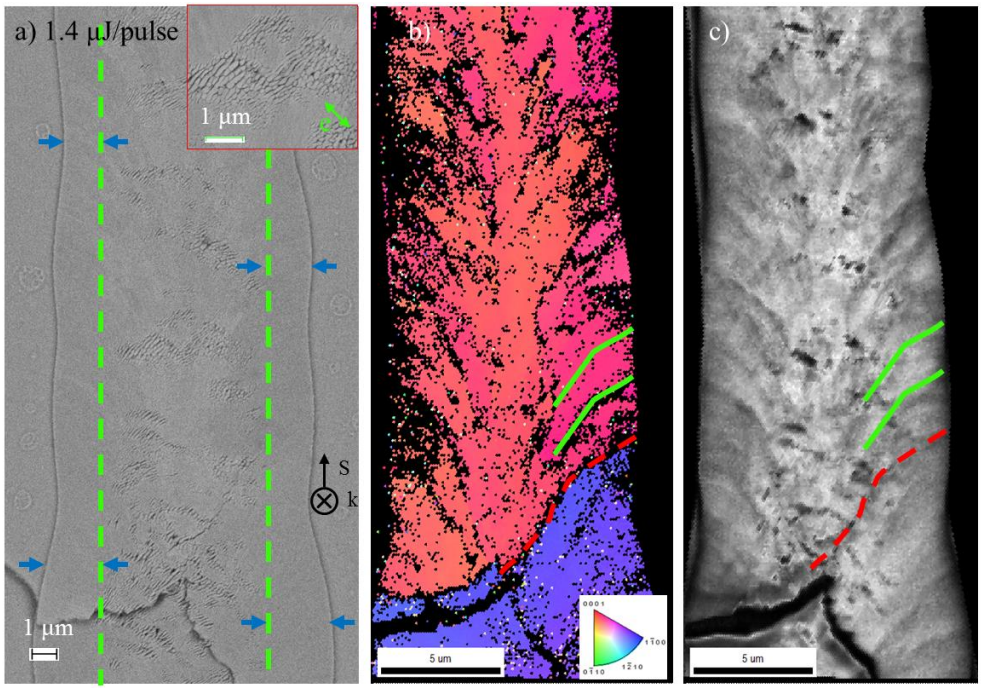


Figure 6. Crystallization morphology in the plane perpendicular to the laser propagation in regime 3. a) SEM image b) EBSD map and c) image quality (IQ) map of fs laser-induced nanostructures in regime 3 of LNS glass. The color in EBSD map is based on $LiNbO_3$ space group (i.e. R3c), coding along writing laser propagation direction. Laser polarization direction (marked by green e) is indicated by the green double arrow (45° off the scanning direction), k is the laser propagation direction and S is the scanning direction. The blue arrows indicate the smooth crystallization zone. The green dashed lines marked the nanostructure boundary. The green curves illustrate a bouquet-like structure, formed by alternation of the crystallized and amorphous region. The red dashed line displayed the grain boundary. Other parameters: $32.5Li_2O$-$27.5Nb_2O_5$-$40SiO_2$ (mol %), 1030 nm, 300 fs, 1.4 μJ/pulse, 500 kHz, 5 μm/s, and focus depth 300 μm in air.

The EBSD map (**Figure 6**b) displays that the crystallization can change the orientation along the scanning direction. A clear grain boundary is illustrated by red dashed line in **Figure 6**b. We also found a bouquet-like structure that is formed by alternation of the crystallized and amorphous region (illustrated by green curves in **Figure 6**b). The bouquet opens in the direction of the scanning.

To have more details on fs laser-induced crystallization, image quality (IQ) is given in **Figure 6**c. For details of the IQ, please refer to the experimental section. We can clearly see the boundary between two zones with different crystalline orientation (illustrated by red dashed line

in **Figure 6**b and **Figure 6**c). Meanwhile, the bouquet-like structure observed in EBSD can be also clearly seen in the IQ map (**Figure 6**c).

When increasing the pulse energy (i.e. 1.8 μJ/pulse at **Figure 7**a), nanostructure, oriented perpendicular to laser polarization direction, is again observed at the centre of irradiated lines surrounded by smooth crystallization region (clearly shown by red rectangle in **Figure 7**a). The bouquet-like structure becomes clearer (illustrated by green lines in **Figure 7**a).

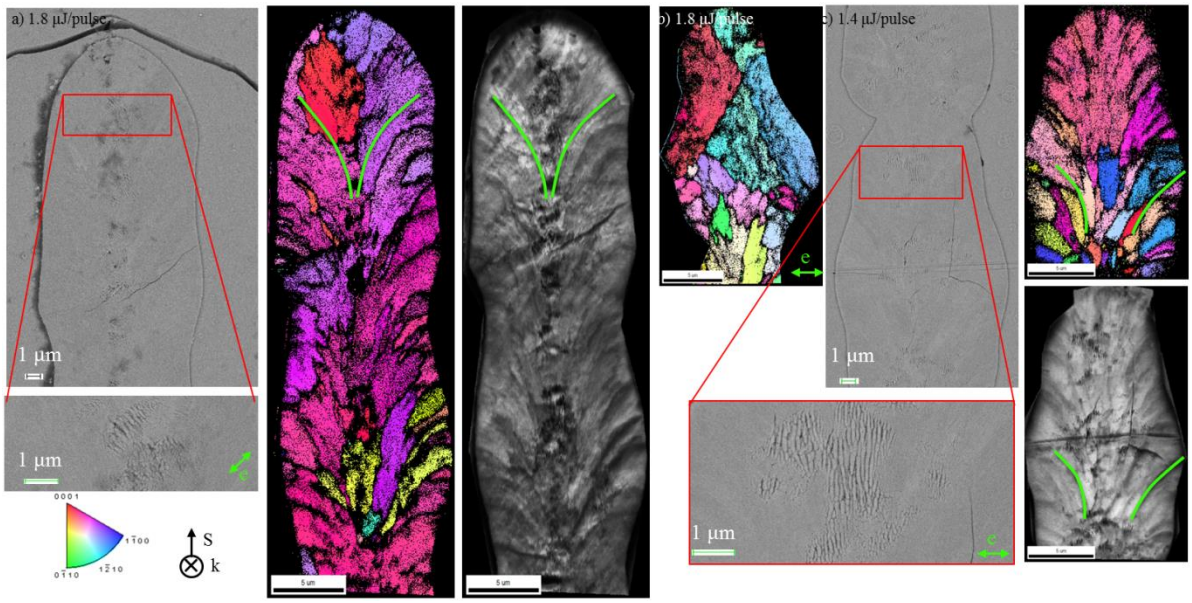


Figure 7. fs laser-induced nanostructures in regime 3 at 2 pulse energies and writing laser polarization direction: a-b) 1.8 and c) 1.4 μJ/pulse. Fig a) left and fig c) left are SEM images; fig a) middle, fig b) and fig c) right top are EBSD maps, fig a) right and fig c) right bottom are image quality (IQ) maps. The color in EBSD map is based on $LiNbO_3$ space group (i.e. R3c), coding along writing laser propagation direction. Laser polarization direction is indicated by green e and the green double arrows in each image, k is the laser propagation direction and S is the scanning direction. Other parameters: $32.5Li_2O$-$27.5Nb_2O_5$-$40SiO_2$ (mol%), 1030 nm, 300 fs, 500 kHz, 5 μm/s, and focus depth 300 μm in air. The green curves marked a bouquet-like structure, formed by alternation of the crystallized and amorphous region.

It is worth noting that, when the scanning direction is perpendicular to writing laser polarization direction, the crystallization orientation tends to be more disordered **(Figure 7**b). Similar results are also obtained when decreasing the pulse energy (**Figure 7**c).

We can also note that the width of the crystallized area does not coincide with the width of the beam (that we track by organized nanostructure) at the difference with regime 2. It is larger.

A focus on cross-sections in regime 3

The morphology of the cross section in regime 3 has been already described in our previous publications for lower repetition rate [3]. An example is given in **Figure 1** at 300 kHz. We can see that for low energy part of the regime 3, there are large grains throughout the width of the cross section but with area without crystals in the head of the laser track shaped like twizers of lobsters revealing different mechanisms. This will be an important point in the discussion. For larger energies, these morphologies disappear and larger grains propagate.

At 500 kHz repetition rate, the examination of the cross section of the line (i.e. perpendicular to writing direction), reveals more complex structures appears but nevertheless with some similarities with the above observations, including core-shell structure in the head or along the body of the laser trace (red dash line in **Figure 8**a). It is worth noticing that the core part exhibits nanostructure whereas the outer part not. As marked with green dash circle in **Figure 8**b, secondary focus was observed along the laser propagation direction. Interestingly, we also found non crystallized areas in the centre of the laser track (marked by red arrow in **Figure 8**c and **Figure 8**d), without crystallization formation. No matter the writing direction is (e.g. along +X direction for **Figure 8**a and **Figure 8**b or +Y for **Figure 8**c and **Figure 8**d), when the writing configuration is parallel (i.e. same direction of scanning and polarization), large grains are observed (illustrated by red dot circle in **Figure 8**c). But for perpendicular configuration, the orientation of crystals is more disordered. It indicates that the polarization plays an important role in the crystal formation even at high pulse energy (i.e. regime 3 of LNS glass). It is worth to

mention that at this large focus depth (e.g. 610 μm), the laser-glass interaction region is enlarged along laser propagation direction.

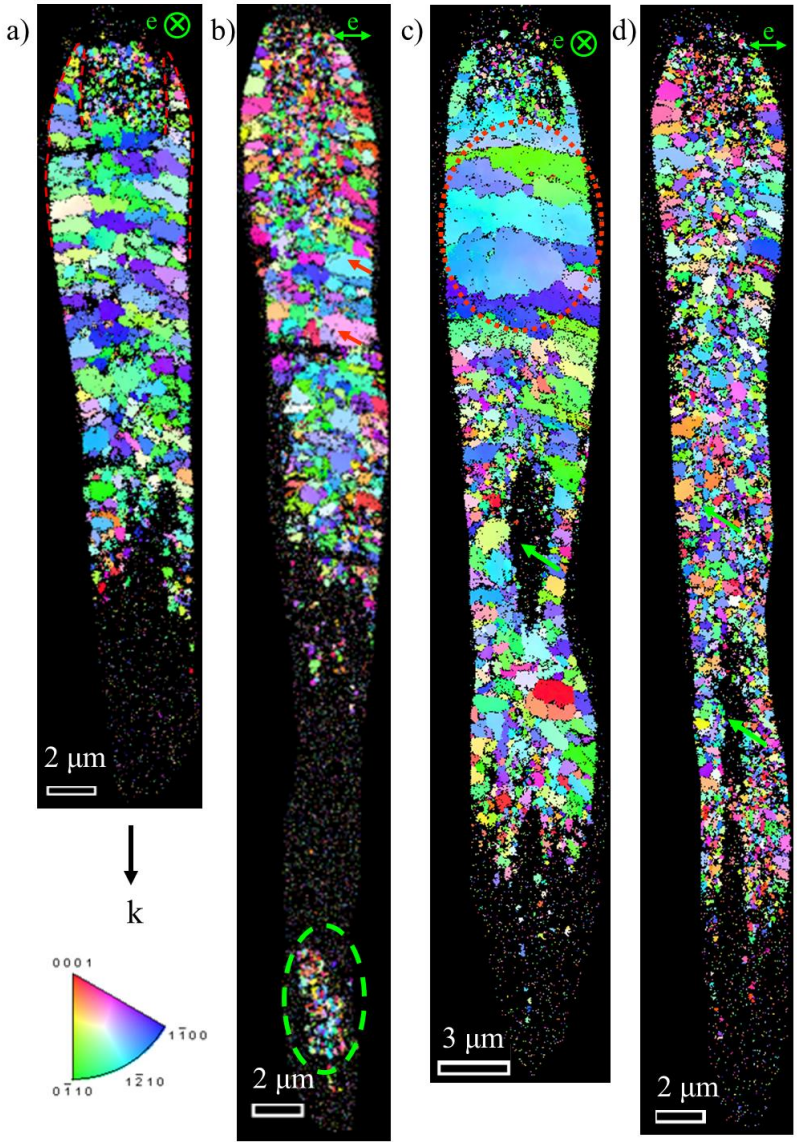


Figure 8. EBSD maps of cross section of laser tracks (i.e. perpendicular to writing direction) varying the scanning and the polarization directions: a-b) along +X direction and c-d) along +Y direction. a and c) are parallel writing configuration (writing direction is parallel to laser polarization direction); b and d) are perpendicular writing configuration (i.e. writing direction is perpendicular to laser polarization direction). The color in EBSD map is based on $LiNbO_3$ space group (i.e. R3c), coding along writing direction. Laser polarization direction (marked by green e) is indicated in each image. Other parameters: $33Li_2O$-$33Nb_2O_5$-$34SiO_2$ (mol%), 1030 nm, 300 fs, 500 kHz, 1.7 μJ/pulse, 5 μm/s, focal depth 610 μm in glass. The laser came from the top (illustrated by k).

Last observation to perform: if we have pointed out previously that laser polarization allows rotating nanocrystals in regime 2, here, we point out that it plays also a role in the regime 3. When this polarization direction is parallel to the scanning direction, the grains can be large and even it can exist only one. When the polarization is perpendicular, there are two areas of crystallization (see **Figure 5**). At the periphery, there are larger grains than at the center. As we can see in **Figure 8**, "the periphery different from the center" is a character of regime 3 at high energy. We observe also a laser track width much smaller leading again to think that the thermal effect is smaller in perpendicular configuration and thus that the light energy absorption is smaller. The reason of such a phenomena will be discussed at the end of section below.

3.5 Control of the birefringence slow axis orientation

Considering that the linear birefringence is an important parameter in fabricating optical components, polarized light microscopy was used to determine the birefringence properties of irradiated line if any. When lines were rotated along the axis parallel to laser propagation direction (i.e. k direction shown in **Figure 9**, an intensity fluctuation of irradiated line is observed (with period of 90°). In contrast, the non-irradiated area is stable (it remains totally dark).

As illustrated in **Figure 9**a and **Figure 9**b, the intensity of birefringent lines reaches the maximum when the writing laser polarization direction (shown by the green double arrows between corresponding two lines) is oriented at 45° between the crossed polarizers (illustrated by A and P in the right side), but is at the minimum value when the writing laser polarization direction is parallel or perpendicular to them. This result indicates the birefringent property of irradiated lines. In particular, the neutral axes of irradiated lines are parallel and perpendicular to the laser polarization direction.

Optical path differences ranging from a fraction of a wavelength up to several wavelengths can be estimated by various retardation plate methods (Senarmont, Berek, Babinet-Soleil), which is suitable in our case [51]. Here, a full-wave retardation plate (530 nm) was used to determine the slow axis orientation of crystallized lines in the plane perpendicular to laser propagation direction. This full-wave retardation plate (λ) is placed with its own slow axis in a diagonal position with respect to the crossed polarizors. The isotropic background (non-irradiated glass matrix) appears magenta; when lines appear blue, this indicates that slow axis of the material and the full-wave retardation plate is aligned; yellow means the slow axis of line is perpendicular to the slow axis of the full-wave retardation plate [72]. As illustrated in **Figure 9**c-d, the slow axis orientation of irradiated line is writing laser polarization direction dependent i.e. slow axis is always perpendicular to the writing laser polarization direction (marked by green double arrows in **Figure 9**a and **Figure 9**b). This result is consistent with the one obtained from the quantitative birefringence microscopy [51]. It shows that by simply adjusting the laser polarization direction, the birefringence properties (e.g. the slow axis orientation) of irradiated lines can be controlled.

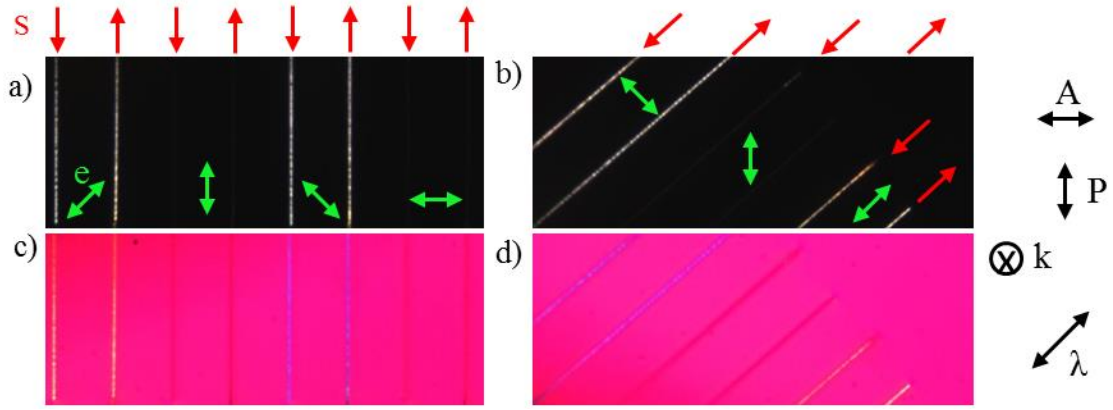


Figure 9. Images of irradiated lines taken between crossed polarizers: a-b) before and c-d) after inserting a full-wave retardation plate. The analyzer and polarizer are denoted as A and P; respectively. Full-wave retardation plate is indicated as λ (double-arrow indicates the direction of slow axis). The distance between each line is 50 μm. k is the laser propagation direction, S is the scanning direction (marked by red arrows), and e is the writing laser polarization direction (illustrated by green double arrows). Other parameters: $32.5Li_2O$-$27.5Nb_2O_5$-$40SiO_2$ (mol %), 1030 nm, 300 fs, 250 kHz, 0.8 μJ/pulse, and 5 μm/s.

DISCUSSION

4.1 Summary of fs laser-induced crystallization in LNS glasses

From the results discussed above, it is demonstrated that writing laser polarization plays a significant role in the crystallization process.

In regime 2, the laser polarization allows orienting the polar axis of crystals (polar axis avoids to be along laser polarization direction). The phase separation imposed by thermodynamics in the chosen laser conditions (i.e. scanning speed low enough, deposited power large enough), produces an amorphous counter phase that is nanostructured by light. The nanostructure is self-organized in the whole volume of the crystallized volume indicating that the beam covers the whole crystallized volume. In addition, this nanostructure is also oriented by the laser polarization as for nanogratings in SiO_2 or GeO_2 glasses [73].

In regime 3, for high pulse energy, the writing configuration (the relative orientation of the laser scanning and the laser polarization) is important in controlling the final crystallization morphology. For parallel configuration, there are large grains that may extend throughout the crystallized volume. As we can see in **Figure 10**, Veenhuizen et al. [53] showed that to obtain a single grain with polar axis parallel to the scanning direction is possible when using pulse energy larger than ours (about twice ours) for the same scanning speed. N.B.: if scanning speed is increased, pulse energy can be slightly increased as we see in **Figure 10**. On the other hand, the nanostructure oriented by the laser polarization is always appearing but it does not cover the whole width of the crystallized volume indicating that now the crystallized area is larger than the light beam. The organization of the nanostructure seems not to play a role in the crystallization

morphology as there is no difference in crystal orientation with or without organized nanostructure. This does not mean that light polarization is not playing a role for that regime. In fact, for perpendicular configuration, the crystallization morphology changes (small grains, disordered) and the crystallized volume width is significantly smaller.

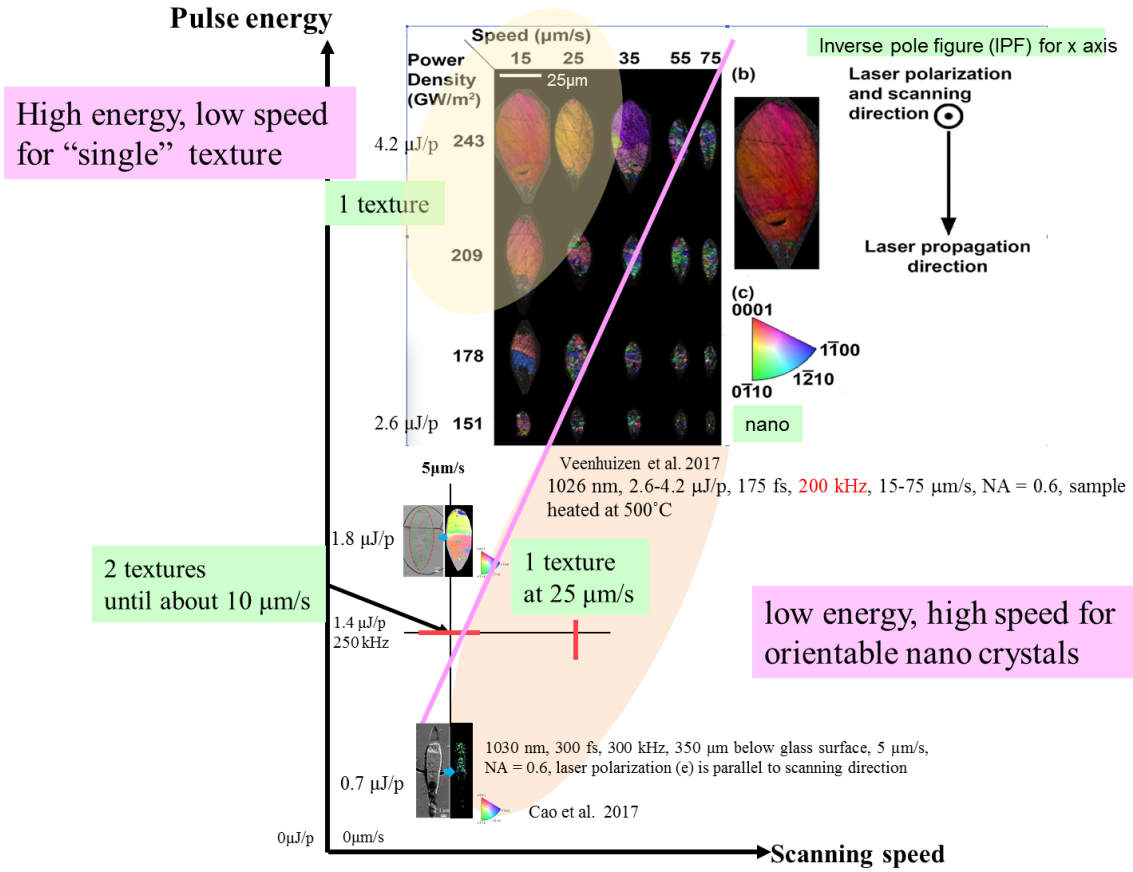


Figure 10. Domains of fs laser-induced crystallization in LNS glasses closed to $30Li_2O$-$30Nb_2O_5$-$40SiO_2$ varying pulse energy and scanning speed. Other parameters 1030 nm, NA = 0.6, 200-300 kHz, parallel configuration. This picture collects results from [3, 53, 60]. The pink line separates symbolically the two regimes: regime 2 with nanocrystal orientation tunability and regime 3 with large grains and even single grain with polar axis aligned with scanning direction.

The above conclusion indicates that with the fs laser, the crystallization is not only achieved by thermal effect, but it is demonstrated for the first time that the vector properties of the light are acting for the first time in the crystallization process. It is nevertheless necessary to be in the crystallization conditions. In such a way, the thermal power deposited is a key parameter as

expected. It is defined by the combination of the pulse energy and the pulse repetition rate. This is shown in **Figure 11** in which we have gathered the various available experiments.

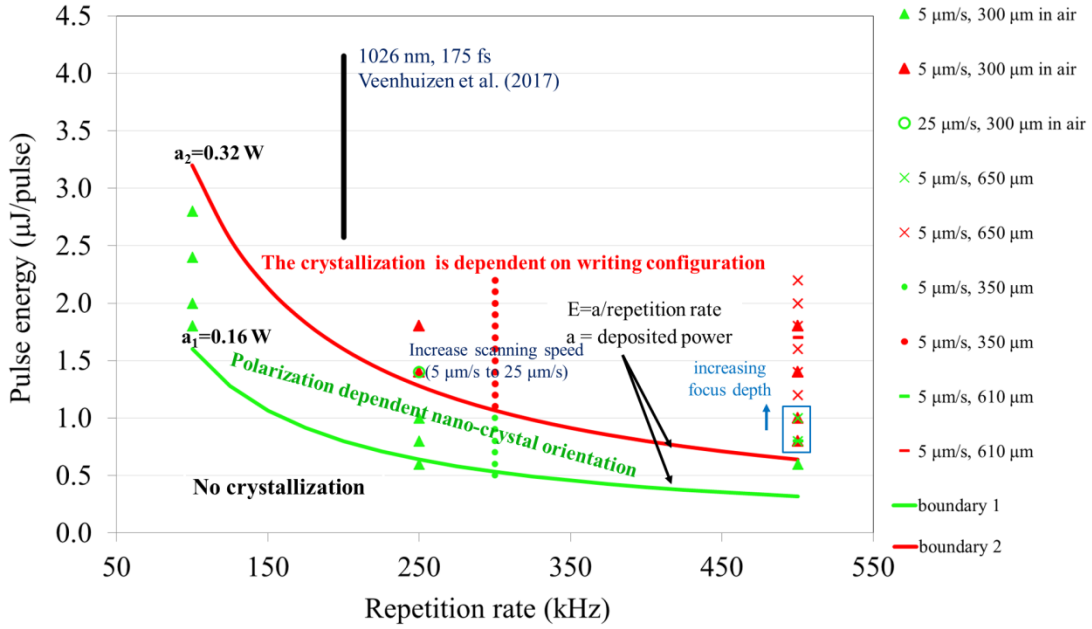


Figure 11. Domain of fs laser-induced crystallization in LNS glasses varying pulse energy and repetition rate at varying scanning speed and focus depth indicated collecting our results and the one from Veenhuizen et al. [53]. Other parameters 1030 nm, 300 fs, NA = 0.6, parallel configuration. The green marks illustrate the regime 2 of LNS glasses and the red marks show the regime 3 of LNS glasses.

We can make the following remarks.

1) Take as an example a 300 µm focusing depth in air (N.B.: this means that the objective has been moved 300 µm from the focusing position at the surface of the sample) and a scanning speed of 5 µm/s for example (i.e. triangle marks in **Figure 11**). With the increase of repetition rate, the energy threshold for obtaining crystallization decreases. We find that the boundary between neighbouring regimes follows the equation: E = a/repetition rate, in which a is therefore an apparent deposited average power (green and red dashed curves). E is the incident pulse energy. For the boundary between regimes 1 and 2, illustrated by green dashed line in **Figure 11**,

the a_1 value is around 0.16 W and for the boundary between regimes 2 and 3, a_2 is around 0.32 W for the investigated LNS glass.

2) The boundary of the crystalline regimes can be adjusted by changing the fabrication parameters (e.g. scanning speed or focusing depth) besides the laser ones. As shown by the green circle in **Figure 11**, with the increase of scanning speed from 5 μm/s to 25 μm/s, for 1.4 μJ/pulse at 250 kHz, 300 μm focus in air, this crystallization regime 3 appears at higher pulse energy. This means that the boundary between regime 2 and 3 increases in energy when the scanning speed is increased. This is clearly seen in **Figure 11**, where we have gathered results according to pulse energy and scanning speed from different authors. This is consistent with a time left to the crystals to grow from a melt like in floating zone technique [74]: the speed of scanning should be lower than the intrinsic speed of growth.

In the other hand, with the increase of focus depth, the boundary between regime 2 and 3 appears at higher energy: e.g. at 500 kHz, we get 0.6 μJ/pulse for 300 μm in air (triangles in**Figure 11**), 0.8 μJ/pulse for 610 μm (crosses in **Figure 11**) and 1.0 μJ/pulse for 650 μm (dashes in **Figure 11**). This is consistent with the expected extension of the focal volume due to spherical aberration.

4.2 Growth dynamics

4.2.1 The temperature distribution

In silica or borosilicate glass, Eaton et al. [75] shown that at low repetition rate (e.g. 100 kHz), thermal diffusivity can carry the heat away from the focus before arriving the next pulse at a timescale of 10 μs. So, the time left at high temperature is very short and the average temperature not large enough for allowing crystallization. However, when the period between two

consecutive pulses is smaller than thermal diffusion time on a length comparable to the beam radius (i.e. w_0^2/D_θ, with D_θ the thermal diffusivity, we get ca. 1 µs in solid oxides), heat accumulation occurs. This means that the minimum and the maximum clearly visible pulse after pulse (schematized in **Figure 12**a by the bistre shaded area), increase on time. But with large number of pulses (larger than a few tens), a steady state mode can be reached (illustrated in **Figure 12** left). So, even if the temperature at one place is oscillating, the maximum and the minimum one does not change anymore if the scanning speed is low enough. If we define an average temperature on the period with the following expression:

$$\bar{T}\left(\vec{r},t_i\right)=\int_{period} T\left(\vec{r},\tau,t_i\right)\frac{d\tau}{period}$$

We can see that for repetition rate large enough, at the steady state, the spatial distribution $\bar{T}\left(\vec{r},\infty\right)$ tends to the one of a CW laser [75-78].

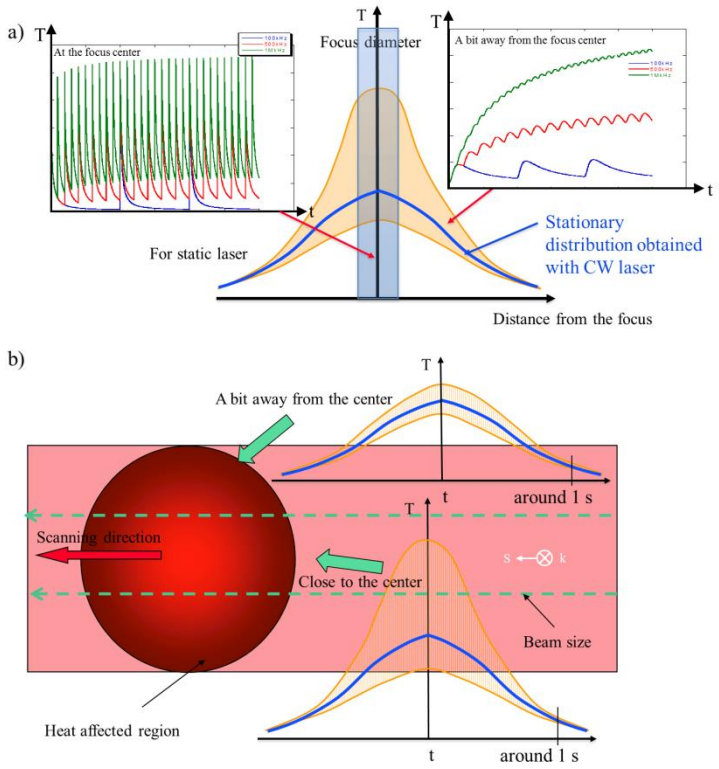


Figure 12. a) Schematic of the spatial temperature distribution produced by a static laser as a function of the distance from the focus center. The left part show the variation of the temperature at the focus center and the right part illustrates a position a bit away according to repetition rate. Note the large variation at the center and the strong damping when further from the center. The blue shaded area symbolizes the approximated beam width. The bistre shaded area is the amplitude of the temperature variation at the steady state. The blue curve is the average stationary distribution similar to the one obtained with CW laser. b) Time evolution of the temperature for a fixed point according to the distance from the focus center in scanning mode. The red area symbolizes the scanning beam, arbitrary limited.

This average temperature distribution is schematized by the blue curve in **Figure 12**a. Note that this last curve is, at the center, closer to the minimum temperature curve as the temperature decrease on time just after the pulse is very fast. Due to these properties, we can control the temperature distribution on time and in space by using fs laser like almost a continuous localized heating source.

Another useful remark for the discussion is that this temperature distribution will be still valid in scanning mode providing that the scanning speed is not too fast. For fulfilling this condition,

the scanning speed should be smaller than the thermal diffusion speed (that we consider again within the beam radius) i.e. speed < D_θ/w_0 . As D_θ/w_0 is of the order of 10 cm/s whereas the scanning speed is not larger than 100 μm/s in ours experimental conditions, so, we can use a static temperature distribution.

The scanning speed itself is limited by the crystallization speed. Fokin et al. [79] demonstrated that for silicate glasses, the maximum crystal growth rates tends to decrease with the increase of reduced glass transition temperature, T_{gr} (defined as T_g/T_m, where T_g is the glass transition temperature and T_m is the melting or liquidus temperature). For example, $2BaO\text{-}TiO_2\text{-}2SiO_2$, (T_{gr}=0.574) crystallizes fresnoite at 430 μm/s, $Li_2O\text{-}2SiO_2$ (T_{gr}=0.557) is 70 μm/s, and $36Na_2O\text{-}64SiO_2$ (T_{gr}=0.629) is 1.58 μm/s. It shows that the growing rate is at the scale of ~1-100 μm growth for the time of a 1s thermal treatment depending on the glass system. The scanning speed is chosen in the range of the typical crystal-growth velocity (i.e. few μm/s) according to the formed crystals [31]. Saito et al. [32] found that crystallized lines cannot be constructed at 1 μm/s but 0.5 μm/s for $15K_2O\text{-}15Sm_2O_3\text{-}70P_2O_5$ glass. With the decrease of writing speed, the heated region caused the formation of a stable structure with a layer at the solid-liquid interface between a part of the polycrystal and the heated zone [23], which is suitable for single crystal or single-crystal-like structure formation.

Now, we can examine the time evolution of the different parts of the glass on the course of the scanning beam (**Figure 12**b). For a point closed to the center of the line, it crosses the center of the beam during its course and thus experiences the largest temperature fluctuation and the largest average temperature variation. For a point away from the center, fluctuations are weaker and the temperature variation is smaller.

4.2.2 Nucleation and crystal growth

Glass is thermodynamically unstable (non-equilibrium). However, because of the low kinetics at temperature small enough (i.e. high viscosity inhibits structural rearrangements) glass structure is frozen. If temperature is increased during a time long enough, relaxation of the glass structure occurs and the glass can evolve to crystalline state. Traditional model assumed that crystallization is a two-step process: nucleation and crystal growth. Classical Nucleation Theory is a simple theory for understanding nucleation of a thermodynamic phase in a liquid or glass (frozen liquid). In the case of homogeneous nucleation, this one occurs because of the thermal fluctuation of the chemical composition. The nucleation occurs anywhere in the phase into consideration. For inhomogeneous nucleation, it occurs on structural defects (e.g. cracks, seeds). Then, nuclei grow in a similar way for both cases. There are distinct kinetics for the nucleation and the growth.

For the homogeneous nucleation, nuclei are formed from chemical composition fluctuations. Some of the nuclei, the ones larger than a critical size, are stable and may experience further growth [80]. The stationary nucleation rate I(T), describing the number of nuclei per time unit at a given temperature is written as [80]

$$I(T) = \frac{dn}{dt} \propto exp\left(-\frac{\Delta G_D}{k_B T}\right) exp\left(-\frac{\Delta G^*}{k_B T}\right)$$

In which, ΔG_D is the activation energy to cross the glass-crystal interface (kinetic barrier) and this activation energy is related to a diffusion coefficient. ΔG^* is the energy barrier to form a nucleus stable to grow. k_B is Boltzmann's constant, and T is the temperature.

When temperature is at or larger than melting temperature (T_m), the growth rate is zero. When temperature is close to T_m, ΔG^* is high, which will play a dominant role in the nucleation rate

(i.e. very low). But the diffusion term is high at this temperature. With the decrease of temperature, the possibility of forming seeds is increasing (because ΔG^* decreases). However, the viscosity of material increases sharply, restricted atom movement and inhibited the ordered crystal structures formation, thus the nucleation rate is decreasing. In that case, there is an optimal temperature for obtaining the maximum nucleation rate. When the temperature is close to T_g, ΔG^* decreases and nucleation rate increases sharply, which might achieve a maximum nucleation rate when ΔG^* and ΔG_D are at same magnitude order (schemed in **Figure 13**a).

The rate of crystalline growth C(T), corresponding to critical nuclei growth with radius larger than r* is given as [80]

$$C(T) = k_{lc} - k_{cl} = f\lambda v \exp\left(-\frac{\Delta G_D}{k_B T}\right)\left[1 - \exp\left(-\frac{\Delta G_V}{k_B T}\right)\right]$$

Where f is the fraction of sites on the crystal surface, available for attachment; ΔG_V is the difference in free energy per unit volume between liquid or amorphous and crystal. Note that ΔG_D is not necessarily identical to the nucleation activation energy discussed above.

Usually, at higher temperature, crystal growth rate is larger than nucleation rates. The nucleation happens at lower temperature than crystal growth (see **Figure 13**a). As the two steps combines for homogeneous crystallization, the fraction of crystalline part of the glass x_c is obtained by the time integration of the crystallization rate $\frac{\delta x_c}{\delta t}$ issued from system resolution of the successive reactions. We get $x_c\left(\vec{r}\right) = \int_{treatment}\int_{time} \frac{\delta x_c}{\delta t}\left(t, T\left(\vec{r}, t\right)\right)dt$ for each place refered at coordinate. When temperature is not time dependent (isothermal annealing), the experiment leads to what it is called time temperature transformation curve (TTT curve), which is schemed

in **Figure 13**b in black. When the nucleation is heterogeneous, only the growth rate has to be taken into account and we obtain a curve like the one in red in the same figure.

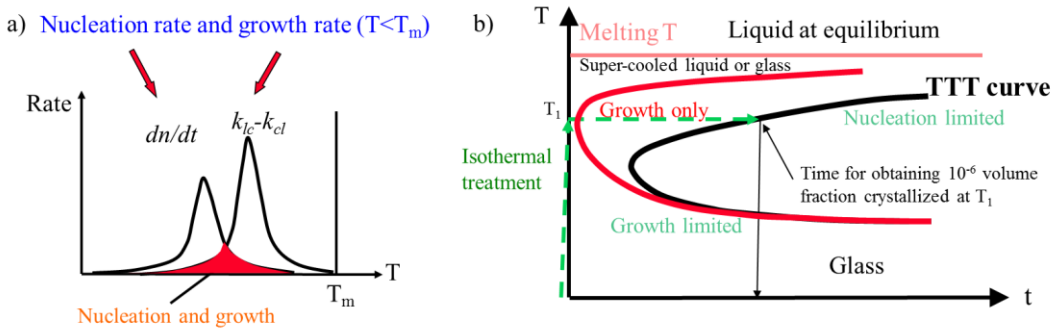


Figure 13. a) Scheme of the nucleation and growth rates. b) TTT curve obtained by time integration of the previous rates.

4.2.3 TTT and CCT curves and maximum growth rate

However, in our case, the thermal treatment is not isotherm but more complex. We will see that sometimes it starts from the melt. One simplified treatment can be indicative for us: the constant cooling. In that case, the temperature is decreased from the melt at T_m at a constant rate (marked by red circle in **Figure 14**a). The time integration of the crystallization rate in that case leads to continuous cooling transformation (CCT) curve.

For more complex thermal history, the crystallization region may vary a bit but we will not consider this effect as the chemistry will be the same. What we have to note here, is that the transformation curve delimit a domain of crystallization that is reached after a time depending on the cooling curve and that there is a temperature domain below the melting temperature for which the crystallization rate is the largest.

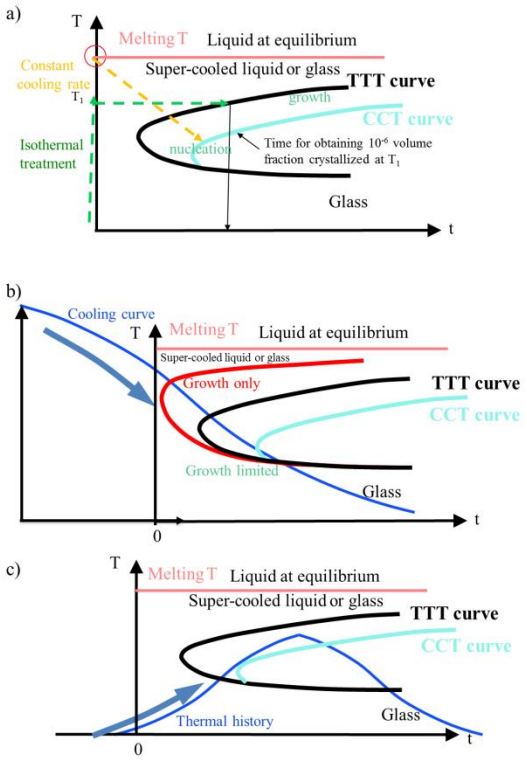


Figure 14. a) The TTT and CCT curves (CCT curve appears shifted from the TTT one a little to the downward right. This is because lower growth rate is integrated during the cooling process from the melt to a given T. Thus the time required for obtaining the same amount (e.g. 10^{-6}) is larger; b) For places experiencing maximum average T larger than T_m c) For places experiencing maximum temperature smaller than melting temperature.

Now, consider the evolution of the temperature during beam scanning at the different places of the irradiated area like **Figure 14**b and **Figure 14**c. The temperature rises and then decreases. When the maximum temperature is larger than T_m, just the part below the T_m and during the decreasing stage has to be considered because higher temperature erases the past. The treatment time starts from the T_m. Therefore, cooling curves are drawn and compared to the transformation curves accordingly in **Figure 14**b. The transformation curve to consider depends on the nucleation, if it is homogeneous or not. We will see this point below. For places experiencing maximum temperature smaller than melting temperature, the time origin is not so well defined

and the T(t) curve is drawn in **Figure 14**c, just for fixing the ideas. We see that crystallization occurs without melting and starts under temperature increasing by nucleation.

4.2.4 Interpretation of crystallization dynamics

Now, the interpretation of crystallization dynamics will be discussed in four parts depending on the deposited energy at high repetition rate as following:

1) Low pulse energy (i.e. regime 1 for LNS glass): The irradiation condition is not suitable for crystallization, no crystallization is obtained but there are some permanent modifications of the amorphous area [3].

2) Intermediate low pulse energy (i.e. regime 2 for LNS glass): As shown in **Figure 15** left image, the average temperature is always below the melting temperature and below the maximum growth rate. A solid state transformation occurs. From SEM and EBSD images of the cross section of laser track (**Figure 15** right), only nanocrystals were obtained. Nanostructure is obtained on the whole crystallized volume. This means that the light beam covers all the crystallized area. This means that only the part of the spatial temperature distribution in the beam meets the crystallization area like it is schemed in **Figure 15**. In that case, growth rate is quite low and only nanocrystals appear everywhere after homogeneous nucleation. Nanocrystals are there all orientable with the laser polarization.

When pulse energy is increased slightly, the T(t) curve at the center of the crystallized area can reach a temperature for which the growth is larger and thus larger grains are produced. This is the case for 1.4 μJ/pulse, 250 kHz, 10 μm/s (see **Figure 10** and **Figure 11**) for instance. In that case, the crystals loose the laser polarization sensitivity and show a tendency to orient in another texture i.e. along the direction of scanning (i.e. the main temperature gradient) like with a CW

laser. Such samples may exhibit two textures like we have observed for 25 µm/s, 1.4 µJ/pulse, 250 kHz (see **Figure 10** and **Figure 11**).

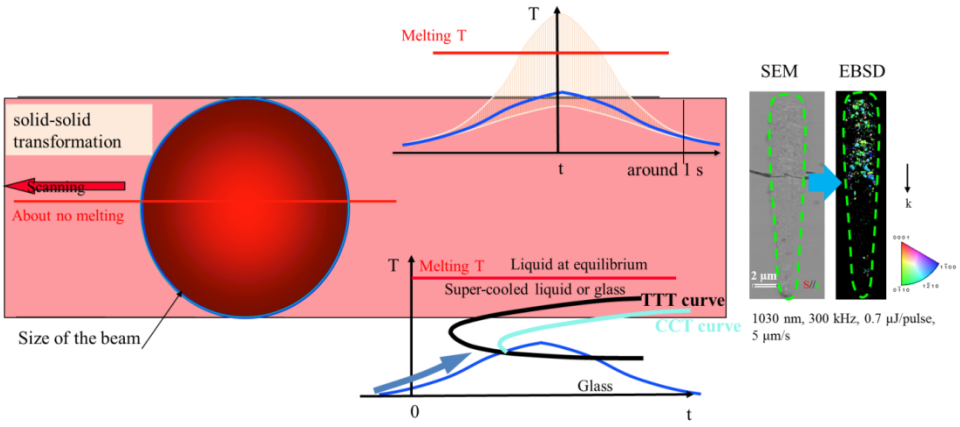


Figure 15. Time evolution of the temperature for a fixed point according to the distance from the focus center in scanning mode at intermediate pulse energy (regime 2 for LNS glass). On the right side are shown the SEM and EBSD images of the cross section of the laser track obtained in the corresponding regime. The color in the EBSD maps is based on $LiNbO_3$ space group, coding along the laser polarization direction.

3) High pulse energy (ca 2 µJ/pulse, i.e. regime 3 for LNS glass for configuration close to parallel one). From the inspection of the nanostructure extend (see **Figure 6** and **Figure 7**), we deduce that the light beam is now not covering the whole crystallized area. The situation is schemed in **Figure 16**. From the computations, we know that the average temperature overcome the T_m. Its location is shown by red lines and a circle in **Figure 16**. Here, the liquid-solid transformation occurs. In contrast, in the surrounding, temperature is lower than T_m, and solid state transformation occurs. The zones with the maximum growth rate are illustrated by the blue curve in **Figure 16**. What is suggested here is that there are two areas, one with solid-solid transformation and one with liquid-solid transformation as it was recently proposed by Savitskii et al. [18] However, we do not see clearly a boundary between these two regions either on EBSD image in the plane of writing (XY plane) or in the cross section (

Figure 1c and d or **Figure 8**). It is worth noticing that **Figure 8** is obtained by polishing and reach the body of the cross section, not the head where a two areas structure appears. So, how to explain the absence of boundary between the two transformation areas? How to explain the bouquet morphology appearing in **Figure 6** and **Figure 7**?

The explanation is illustrated in **Figure 17**. Considering a time t, the crystallization starts from the periphery by homogeneous nucleation at lower temperature than in the center. The crystallization at the center starts from T_m and is limited by the nucleation. As the beam is moving, the temperature in the periphery will increase and the nuclei will grow whereas the center may be delayed waiting nucleation. The dark zone in the top picture of **Figure 17**, giving rise to the bouquet aspect, is amorphous region (green lines). We believe they indicate the shape of the growth front. We suggest that growth propagates from periphery towards the center following these lines. The distance between two green lines would correspond therefore to an effective growth rate resulting from the multiplication of the intrinsic growth rate and the opened time at temperature high enough. So, we can represent this by the following equation:

$$\Delta x_c = \frac{\delta x_c}{\delta t}(T_{max})\frac{\alpha T_{max}}{dT/dt}$$

Where αT_{max} is the range of T on which the growth is active ($\alpha<1$).

As the growth front lines are not parallel, we can deduce that growth rate is smaller at the center. This can be explained by the fact that the cooling rate (i.e. the slope dT/dt) is faster at the center than at the periphery (see **Figure 17**). We have also not to exclude a possible delay to solidification at the center (deformation of the red continuous curve in **Figure 17** near the center)

for explaining the shape of the crystallization curve but this would need additional numerical modeling for being really convincing.

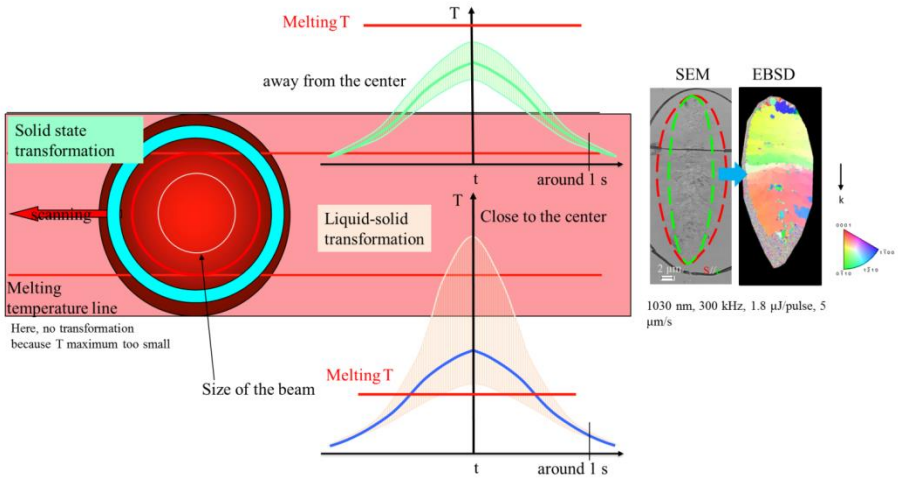


Figure 16. Time evolution of the temperature for a fixed point according to the distance from the focus center in scanning mode at high pulse energy (regime 3 for LNS glass). The right side is the SEM and EBSD images of the cross section of the laser track obtained in the corresponding regime. The color in the EBSD maps is based on $LiNbO_3$ space group, coding along the laser polarization direction. Blue dashed line in the SEM image is the beam boundary and red dashed line is the crystallized volume boundary.

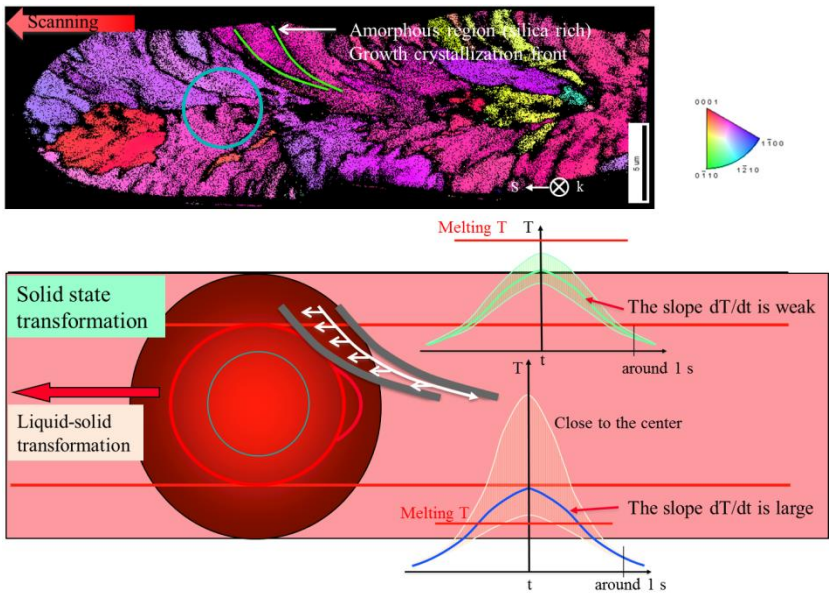


Figure 17. Interpretation of the morphology obtained at high pulse energy (regime 3 for LNS glass) in the plan perpendicular to laser propagation direction (XY plane). The blue circle indicates the beam size inside which the temperature is almost homogeneous. The green curves illustrate the bouquet morphology. The picture at the top is taken from **Figure 7**a.

4) Very high pulse energy (ca 4 μJ) is an extreme case of the previous one. The width of the crystallized area is large e.g. 32 μm at 4.2 μJ and 25 μm/s (illustrated in **Figure 11**). In comparison, the beam size is of the order of 6 μm at 4 μJ. Therefore, the thermal-affected area is much larger than the beam size.

The temperature is again above T_m at the center of the modified area. Its location is shown by red lines and a circle in **Figure 16**. Between these ones, the temperature is far larger than T_m. We can expect the occurrence of a liquid-solid transformation in the central area. In contrast, away from the center, beyond the red lines, the maximum temperature is lower than T_m and we can expect the occurrence of a solid-solid transformation. The zones with the maximum growth rate are illustrated by the blue curve in **Figure 16**.

On the other hand, this case was already studied by Stone et al. [81] recently. They saw that the crystallization front is like the yellow curve drawn in **Figure 18**. It moves in the scanning direction. In addition, considering that growth rate usually is maximum along c axis in perovskite materials, this explains that the c-axis is oriented along the scanning direction.

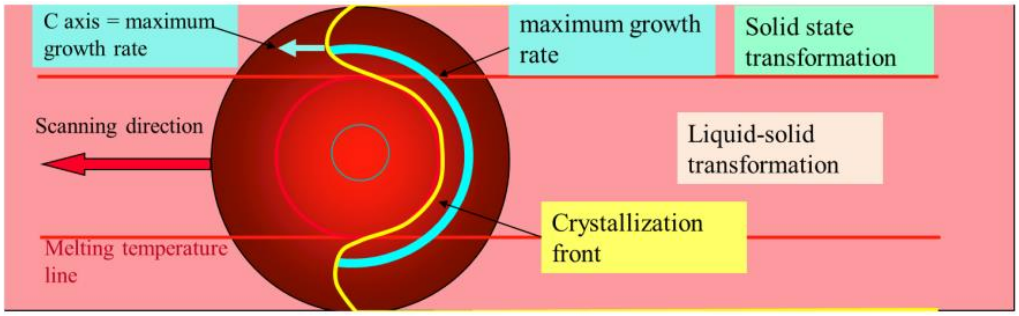


Figure 18. Time evolution of the temperature for a fixed point according to the distance from the focus center in scanning mode at very high pulse energy (ca 4 μJ) and the interpretation of the formed single texture.

4.2.5 Back on the non-uniform morphology of the laser tracks cross sections in regime 3

We mentioned the strange aspect of the "head" of the cross section in **Figure 1** and **Figure 8**. We can now suggest explanation. This is described in **Figure 19** using again the example of **Figure 1**. The tweezer-like shape of the head of the laser track is formed by solid-solid transformation like we have already mentioned above. The body of the trace is resulting from a liquid-solid transformation. Between these two cases, when the energy is lower, such that the maximum temperature of the treatment curve is just slightly above the melting temperature, the cooling is faster and may not reach the crystallization domain in the Time-Temperature transformation plane. This is an intermediate situation.

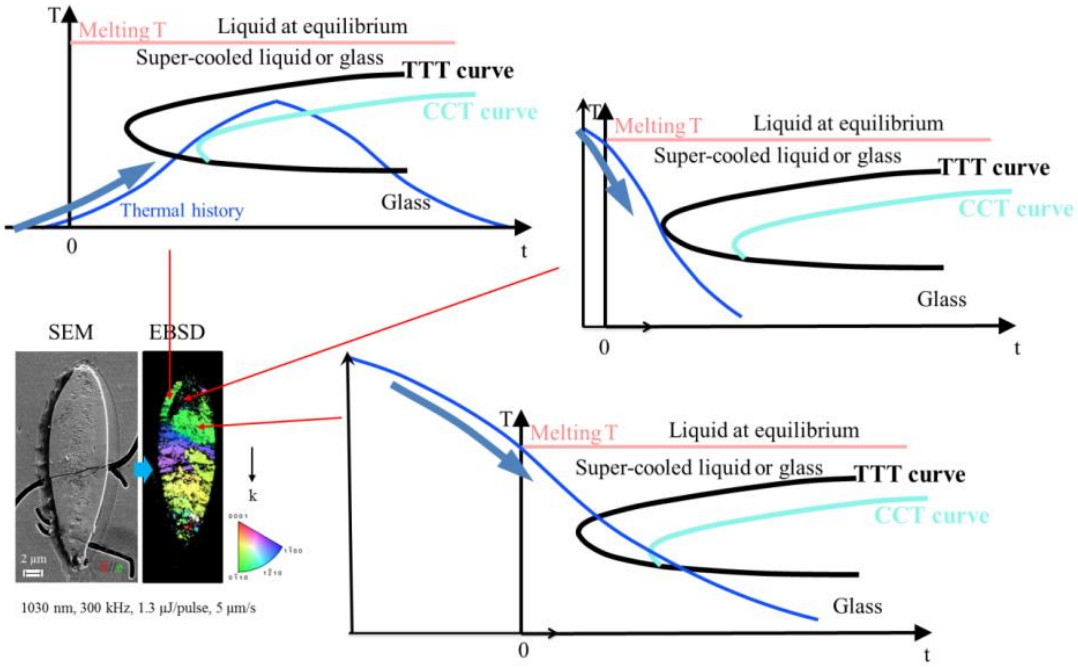


Figure 19. Interpretation of the presence of non-crystallized area in the section of the laser traces.

4.2.6 Influence of the laser polarization orientation in Regime 3

In section 3.3, we have observed for a parallel writing configuration (linear polarization parallel to the scanning direction) that the grains are at the micro scale whereas for a perpendicular configuration the grains are at the nano scale. In addition, the modified zone is

large in the first case showing a large thermal effect whereas it is smaller in the second case. What could be the origin of such effect?

According to the pulse energy, the beam size is firstly defined primarily by the focusing strength of the lens and the non-linear index but also by the resulting electron density. This last one itself depends on the multiphoton absorption. But multiphoton absorption changes also along the number of pulses as first pulses create defects and nanocrystals which probably introduces energy levels in the gap and contributes to decrease it. Would it be in this process some anisotropies? We have to consider here the case of high energy pulses. Two mechanisms can be considered: inhomogeneous nucleation and propagation from crystallization front so sensitive to the scanning direction and homogenous nucleation that is not sensitive to scanning direction. On the other hand, due to the anisotropy of the crystal, multiphoton absorption could be higher for a nanocrystal orientation than for another. At the beginning of the irradiation, nanocrystals are randomly oriented; some of them are parallel to laser polarization. On these places, the electron excitations are intense. If, these nanocrystals are oriented (for simplifying) parallel to the scanning direction, they are favored to grow (parallel configuration) and the electron density increases. Therefore, the width of the beam increases. In the case of perpendicular configuration, the nanocrystals are not favored to grow and the nanocrystal orientation is random and the electron density remains lower, the beam width remains smaller.

CONCLUSIONS

We have systematically studied the fs laser irradiation induced crystallization in LNS glasses. We analyzed the crystallization morphology of the laser traces and we classified them into three regimes using results obtained for repetition rate between 100 kHz and 500 kHz. We designed the different domains in the plan energy-pulse repetition rate and find that a first boundary can be

drawn based on an apparent deposited power of 0.16 W and a second one involving a power of 0.32 W. Beyond the first boundary, crystallization occurs. Below the second boundary, it is only nano-crystals but there are orientable with the laser polarization. We interpret the nano-crystallization and the coexistence of organized nanostructure and texture by a solid-solid transformation using the nucleation and growth theory. Above the second boundary, the pulse energy is large enough to melt a part of the center of the laser track. A zone of liquid-solid transformation appears in the center. Another texture appears here that we interpret as driven by the propagation of crystallization from the periphery to the center. This one is not rotatable because driven by temperature gradient and large growth rate. This can lead to single texture at high energy as shown by Veenhuizen et al.[53]. We show also the two regimes in the plane pulse energy-scanning speed and point out that fast scanning allows extending in energy the rotatable nanocrystals domain whereas slow scanning allows to elaborate single texture at low energies.

We have also to underline that due to inhomogeneous crystallization in the cross section (solid-solid and liquid-solid transition) and the different mechanism (nucleation and growth in the first region and growth only in the second), the crystallization rate in the two zones are different: faster in the second than in the first one. We deduce that, the scanning speed should be lower than the crystallization rate of the solid-solid transition.

If we have pointed out previously that laser polarization allows rotating nanocrystals in regime 2, here, we point out that laser polarization play also a role in regime 3. When it is parallel to the scanning direction, the grains can be large and even it can exist only one, but when the polarization is perpendicular, the grains are small and seems randomly oriented, the laser track width is much smaller. If the origin of this process remains a mystery, it shows nevertheless that the process involved in fs laser irradiation is much beyond a simple thermal effect.

The important fundamental aspect of this work is that light polarization appears to be a new "button", which we can adjust in solid phase to design, control, and orient a material transformation, in short the immaterial acts on the material. In the field of applications (e.g. integrated optics), with further improvements in the fabrication techniques, the application of this work will be useful to achieve 3D multi-functional optical devices such as second harmonic generation waveguides, electro-optics waveguides, all-integrated optical isolators and birefringence-based devices. Beside this, the interpretation suggested in this paper could be useful for managing crystallization induced by CW laser irradiation as many crystal types can be elaborated space selectively in such a way for integrated optics. In particular, it is likely that we can play with non congruent system for producing other physical properties embedded in organized nanostructures.

ASSOCIATED CONTENT

Supporting Information

The Supporting Information is available free of charge on the ACS Publications website.

Optical floating-zone method

AUTHOR INFORMATION

Corresponding Author

*E-mail: bertrand.poumellec@u-psud.fr

Notes

The authors declare no competing financial interest.

ACKNOWLEDGMENT

The authors thank Dr N. Ollier for useful advices and S. Gautier for glass making technics.

ABBREVIATIONS

LNS, lithium niobium silicate; SHG, second harmonic generation; fs, femtosecond; ns, nanosecond; CW, continuous wave; 3D, three dimensions; SEM, scanning electron microscope; EBSD, electron backscatter diffraction; TEM, transmission electron microscopy; NA, numerical aperture; PF, pole figure; IPF, inverse pole figure; IQ, image quality; TTT, temperature transformation; continuous cooling transformation, CCT.

REFERENCES

1. Fernandez, T. T.; Sakakura, M.; Eaton, S. M.; Sotillo, B.; Siegel, J.; Solis, J.; Shimotsuma, Y.; Miura, K., Bespoke photonic devices using ultrafast laser driven ion migration in glasses. *Prog. Mater Sci.* **2018,** 94, 68-113.
2. Liu, X.; Zhou, J.; Zhou, S.; Yue, Y.; Qiu, J., Transparent glass-ceramics functionalized by dispersed crystals. *Prog. Mater Sci.* **2018**.
3. Cao, J.; Mazerolles, L.; Lancry, M.; Brisset, F.; Poumellec, B., Modifications in lithium niobium silicate glass by femtosecond laser direct writing: morphology, crystallization, and nanostructure. *J. Opt. Soc. Am. B* **2017,** 34, (1), 160-168.
4. Honma, T., Laser-induced crystal growth of nonlinear optical crystal on glass surface. *J. Ceram. Soc. Jpn.* **2010,** 118, (1374), 71-76.
5. Teng, Y.; Zhou, J.; Sharafudeen, K.; Zhou, S.; Miura, K.; Qiu, J., Space-selective crystallization of glass induced by femtosecond laser irradiation. *J. Non-Cryst. Solids* **2014,** 383, 91-96.
6. Vigouroux, H.; Fargin, E.; Fargues, A.; Garrec, B. L.; Dussauze, M.; Rodriguez, V.; Adamietz, F.; Mountrichas, G.; Kamitsos, E.; Lotarev, S., Crystallization and second harmonic generation of lithium niobium silicate glass ceramics. *J. Am. Ceram. Soc* **2011,** 94, (7), 2080-2086.
7. Cao, J.; Poumellec, B.; Mazerolles, L.; Brisset, F.; Helbert, A.-L.; Surble, S.; He, X.; Lancry, M., Nanoscale phase separation in lithium niobium silicate glass by femtosecond laser irradiation. *J. Am. Ceram. Soc* **2017,** 100, (1), 115-124.
8. Wang, Y.; Honma, T.; Komatsu, T., Crystallization and photoluminescence properties of α-$RE_2(WO4)_3$ (RE: Gd, Eu) in rare-earth tungsten borate glasses. *Opt. Mater.* **2013,** 35, (5), 998-1003.
9. Komatsu, T., Design and control of crystallization in oxide glasses. *J. Non-Cryst. Solids* **2015,** 428, 156-175.
10. Cao, J.; Poumellec, B.; Brisset, F.; Helbert, A.-L.; Lancry, M., Tunable angular-dependent second-harmonic generation in glass by controlling femtosecond laser polarization. *J. Opt. Soc. Am. B* **2016,** 33, (4), 741-747.

11. Lin, C.; Rüssel, C.; Dai, S., Chalcogenide glass-ceramics: Functional design and crystallization mechanism. *Prog. Mater Sci.* **2018,** 93, 1-44.
12. Wolfram, H.; Beall, G. H., *Glass ceramic technology*. John Wiley & Sons: 2012.
13. Komatsu, T.; Koshiba, K.; Honma, T., Preferential growth orientation of laser-patterned $LiNbO_3$ crystals in lithium niobium silicate glass. *J. Solid State Chem.* **2011,** 184, (2), 411-418.
14. Stone, A.; Jain, H.; Dierolf, V.; Sakakura, M.; Shimotsuma, Y.; Miura, K.; Hirao, K.; Lapointe, J.; Kashyap, R., Direct laser-writing of ferroelectric single-crystal waveguide architectures in glass for 3D integrated optics. *Sci Rep* **2015,** 5, 10391.
15. Shimotsuma, Y.; Mori, S.; Nakanishii, Y.; Kim, E.; Sakakura, M.; Miura, K., Self-assembled glass/crystal periodic nanostructure in Al_2O_3-Dy_2O_3 binary glass. *Appl. Phys. A* **2018,** 124, (1), 82.
16. Honma, T.; Benino, Y.; Fujiwara, T.; Komatsu, T.; Sato, R., Technique for writing of nonlinear optical single-crystal lines in glass. *Appl. Phys. Lett.* **2003,** 83, (14), 2796-2798.
17. Zhu, B.; Dai, Y.; Ma, H.; Zhang, S.; Lin, G.; Qiu, J., Femtosecond laser induced space-selective precipitation of nonlinear optical crystals in rare-earth-doped glasses. *Opt. Express* **2007,** 15, (10), 6069-6074.
18. Savytskii, D.; Knorr, B.; Dierolf, V.; Jain, H., Demonstration of single crystal growth via solid-solid transformation of a glass. *Sci Rep* **2016,** 6, 23324.
19. Shevyakina, D.; Lotarev, S.; Lipat'ev, A.; Priseko, Y. S.; Lepekhin, N.; Sigaev, V.; Kazanskii, P., Local Crystallization of Lithium-Niobium-Silicate Glass by Copper-Vapor Laser Beam. *Glass and Ceramics* **2015**, 1-5.
20. Lotarev, S.; Fedotov, S.; Lipatiev, A.; Presnyakov, M.; Kazansky, P.; Sigaev, V., Light-driven nanoperiodical modulation of alkaline cation distribution inside sodium silicate glass. *J Non Cryst Solids* **2018,** 479, (Supplement C), 49-54.
21. Cao, J.; Poumellec, B.; Brisset, F.; Lancry, M., Pulse energy dependence of refractive index change in lithium niobium silicate glass during femtosecond laser direct writing. *Opt. Express* **2018,** 26, (6), 7460-7474.
22. Sato, R.; Benino, Y.; Fujiwara, T.; Komatsu, T., YAG laser-induced crystalline dot patterning in samarium tellurite glasses. *J. Non-Cryst. Solids* **2001,** 289, (1), 228-232.
23. Miura, K.; Qiu, J.; Mitsuyu, T.; Hirao, K., Space-selective growth of frequency-conversion crystals in glasses with ultrashort infrared laser pulses. *Opt. Lett.* **2000,** 25, (6), 408-410.
24. Komatsu, T.; Ihara, R.; Honma, T.; Benino, Y.; Sato, R.; Kim, H.; Fujiwara, T., Patterning of non-linear optical crystals in glass by laser-induced crystallization. *J. Am. Ceram. Soc* **2007,** 90, (3), 699-705.
25. Honma, T.; Benino, Y.; Fujiwara, T.; Komatsu, T., Transition metal atom heat processing for writing of crystal lines in glass. *Appl. Phys. Lett.* **2006,** 88, (23), 231105-231105.
26. Ihara, R.; Honma, T.; Benino, Y.; Fujiwara, T.; Sato, R.; Komatsu, T., Writing of two-dimensional crystal curved lines at the surface of Sm_2O_3–Bi_2O_3–B_2O_3 glass by samarium atom heat processing. *Solid State Commun.* **2005,** 136, (5), 273-277.
27. Maciente, A. F.; Mastelaro, V. R.; Martinez, A. L.; Hernandes, A. C.; Carneiro, C. A. C., Surface crystallization of β-BaB_2O_4 phase using a CO_2 laser source. *J. Non-Cryst. Solids* **2002,** 306, (3), 309-312.
28. Gupta, P.; Jain, H.; Williams, D. B.; Toulouse, J.; Veltchev, I., Creation of tailored features by laser heating of $Nd_{0.2}La_{0.8}BGeO_5$ glass. *Opt. Mater* **2006,** 29, (4), 355-359.

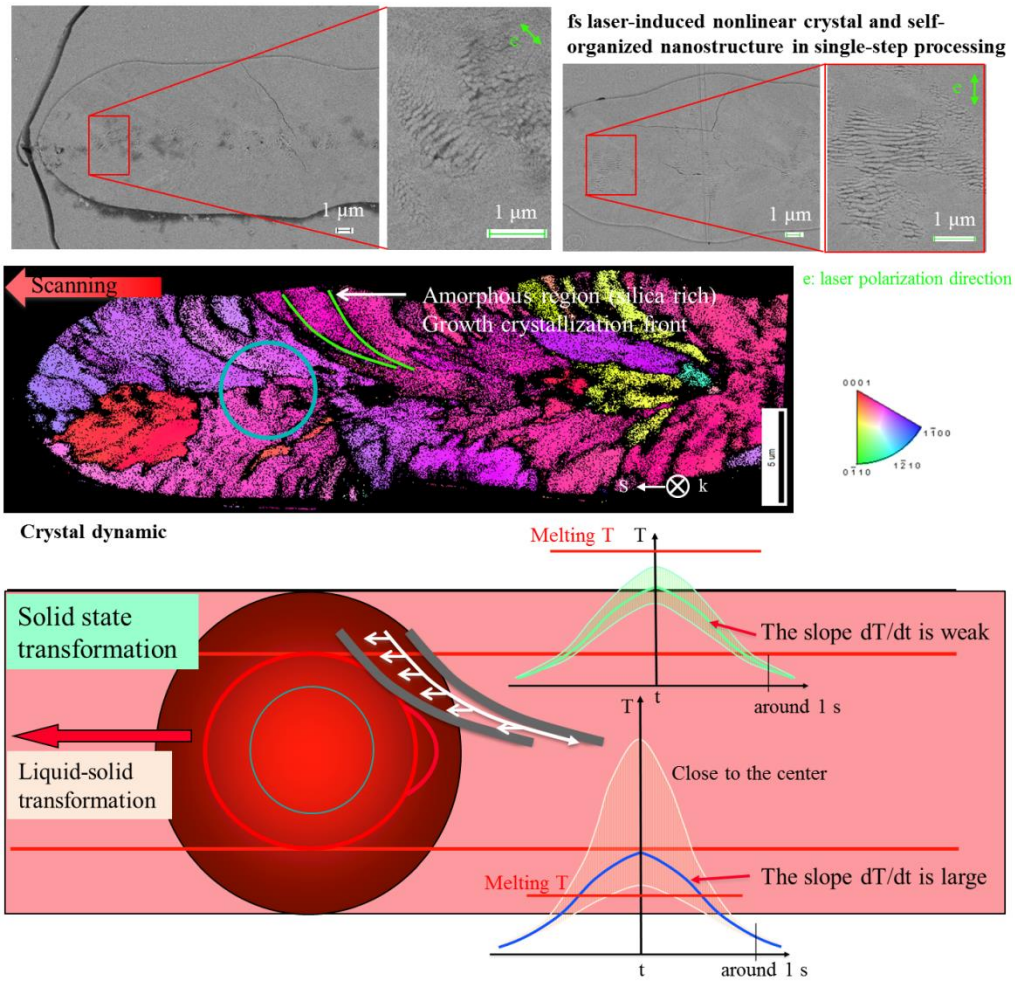
29. Rodriguez, V.; Venkataraman, B. H.; Prasad, N. S.; Varma, K.; Maglione, M.; Vondermuhll, R.; Etourneau, J., Optical diffraction of second-harmonic signals in the $LiBO_2$-Nb_2O_5 glasses induced by self-organized $LiNbO_3$ crystallites. *Appl. Phys. Lett.* **2005,** 87, 3.
30. Chayapiwut, N.; Honma, T.; Benino, Y.; Fujiwara, T.; Komatsu, T., Synthesis of Sm^{3+}-doped strontium barium niobate crystals in glass by samarium atom heat processing. *J. Solid State Chem.* **2005,** 178, (11), 3507-3513.
31. Gupta, P.; Jain, H.; Williams, D. B.; Honma, T.; Benino, Y.; Komatsu, T., Creation of ferroelectric, single-crystal architecture in $Sm_{0.5}La_{0.5}BGeO_5$ glass. *J. Am. Ceram. Soc.* **2008,** 91, (1), 110-114.
32. Saito, M.; Honma, T.; Benino, Y.; Fujiwara, T.; Komatsu, T., Formation of nonlinear optical $KSm(PO_3)_4$ crystals in phosphate glasses by YAG laser irradiation. *Solid State Sci.* **2004,** 6, (9), 1013-1018.
33. Kawasaki, S.; Honma, T.; Benino, Y.; Fujiwara, T.; Sato, R.; Komatsu, T., Writing of crystal-dots and lines by YAG laser irradiation and their morphologies in samarium tellurite glasses. *J. Non-Cryst. Solids* **2003,** 325, (1), 61-69.
34. Wang, Y.; Honma, T.; Komatsu, T., Synthesis and laser patterning of ferroelastic β′-$RE2(MoO_4)_3$ crystals (RE: Sm, Gd, Tb, Dy) in rare-earth molybdenum borate glasses. *Mater. Chem. Phys.* **2012,** 133, (1), 118-125.
35. Abe, M.; Benino, Y.; Fujiwara, T.; Komatsu, T.; Sato, R., Writing of nonlinear optical $Sm_2(MoO_4)_3$ crystal lines at the surface of glass by samarium atom heat processing. *J. Appl. Phys* **2005,** 97, (12), 123516.
36. Hasegawa, S.; Shinozaki, K.; Honma, T.; Dimitrov, V.; Kim, H. G.; Komatsu, T., Dielectric properties of glass-ceramics with $Ba_{1-x}Y_{2x/3}Nb_2O_6$ nanocrystals and laser patterning of highly oriented crystal lines. *J. Non-Cryst. Solids* **2016,** 452, 74-81.
37. Sato, M.; Honma, T.; Benino, Y.; Komatsu, T., Line patterning of $(Sr,Ba)Nb_2O_6$ crystals in borate glasses by transition metal atom heat processing. *J. Solid State Chem.* **2007,** 180, (9), 2541-2549.
38. Sugita, H.; Honma, T.; Benino, Y.; Komatsu, T., Formation of $LiNbO_3$ crystals at the surface of TeO_2-based glass by YAG laser-induced crystallization. *Solid State Commun.* **2007,** 143, (6), 280-284.
39. Honma, T.; Koshiba, K.; Benino, Y.; Komatsu, T., Writing of crystal lines and its optical properties of rare-earth ion (Er^{3+} and Sm^{3+}) doped lithium niobate crystal on glass surface formed by laser irradiation. *Opt. Mater* **2008,** 31, (2), 315-319.
40. Schaffer, C. B.; Brodeur, A.; Mazur, E., Laser-induced breakdown and damage in bulk transparent materials induced by tightly focused femtosecond laser pulses. *Meas. Sci. Technol.* **2001,** 12, (11), 1784.
41. Mao, S.; Quéré, F.; Guizard, S.; Mao, X.; Russo, R.; Petite, G.; Martin, P., Dynamics of femtosecond laser interactions with dielectrics. *Appl Phys A* **2004,** 79, (7), 1695-1709.
42. Du, X.; Zhang, H.; Cheng, C.; Zhou, S.; Zhang, F.; Yu, Y.; Dong, G.; Qiu, J., Space-selective precipitation of ZnO crystals in glass by using high repetition rate femtosecond laser irradiation. *Opt. Express* **2014,** 22, (15), 17908-17914.
43. Stone, A.; Sakakura, M.; Shimotsuma, Y.; Stone, G.; Gupta, P.; Miura, K.; Hirao, K.; Dierolf, V.; Jain, H., Formation of ferroelectric single-crystal architectures in $LaBGeO_5$ glass by femtosecond vs. continuous-wave lasers. *J. Non-Cryst. Solids* **2010,** 356, (52-54), 3059-3065.

44. Stone, A.; Sakakura, M.; Shimotsuma, Y.; Stone, G.; Gupta, P.; Miura, K.; Hirao, K.; Dierolf, V.; Jain, H., Directionally controlled 3D ferroelectric single crystal growth in $LaBGeO_5$ glass by femtosecond laser irradiation. *Opt. Express* **2009,** 17, (25), 23284-23289.
45. Dai, Y.; Zhu, B.; Qiu, J.; Ma, H.; Lu, B.; Cao, S.; Yu, B., Direct writing three-dimensional $Ba_2TiSi_2O_8$ crystalline pattern in glass with ultrashort pulse laser. *Appl. Phys. Lett.* **2007,** 90, (18), 1109.
46. Zhu, B.; Liu, Y.; Ye, S.; Qian, B.; Lin, G.; Dai, Y.; Ma, H.; Qiu, J., Greatly enhanced effect of silver on femtosecond laser-induced precipitation of nonlinear optical crystals in glasses. *Opt. Lett.* **2009,** 34, (11), 1666-1668.
47. Dai, Y.; Zhu, B.; Qiu, J.; Ma, H.; Lu, B.; Yu, B., Space-selective precipitation of functional crystals in glass by using a high repetition rate femtosecond laser. *Chem. Phys. Lett.* **2007,** 443, (4), 253-257.
48. He, X.; Poumellec, B.; Liu, Q.; Brisset, F.; Lancry, M., One-step photoinscription of asymmetrically oriented fresnoite-type crystals in glass by ultrafast laser. *Opt. Lett.* **2014,** 39, (18), 5423-5426.
49. Yonesaki, Y.; Miura, K.; Araki, R.; Fujita, K.; Hirao, K., Space-selective precipitation of non-linear optical crystals inside silicate glasses using near-infrared femtosecond laser. *J. Non-Cryst. Solids* **2005,** 351, (10), 885-892.
50. Honma, T.; Benino, Y.; Fujiwara, T.; Sato, R.; Komatsu, T., Micro-Raman and photoluminescence spectra of Sm^{3+}-doped β-BaB_2O_4 crystal lines written by YAG laser irradiation in glass. *J. Phys. Chem. Solids.* **2004,** 65, (10), 1705-1710.
51. Cao, J.; Mazerolles, L.; Lancry, M.; Solas, D.; Brisset, F.; Poumellec, B., Form birefringence induced in multicomponent glass by femtosecond laser direct writing. *Opt. Lett.* **2016,** 41, (12), 2739-2742.
52. Ogawa, K.; Honma, T.; Komatsu, T., Birefringence imaging and orientation of laser patterned β-BaB_2O_4 crystals with bending and curved shapes in glass. *J. Solid State Chem.* **2013,** 207, 6-12.
53. Veenhuizen, K.; McAnany, S.; Nolan, D.; Aitken, B.; Dierolf, V.; Jain, H., Fabrication of graded index single crystal in glass. *Sci Rep* **2017,** 7, 44327.
54. Maksimova, O. S.; Korzunova, L. V.; Milberg, Z. P., Properties and structure of glasses of the system Li_2O-Nb_2O_5-SiO_2. *Izv.Akad.Nauk Latv.SSR,Ser.Khim* **1975,** 5, 530-534.
55. Weis, R.; Gaylord, T., Lithium niobate: summary of physical properties and crystal structure. *Appl. Phys. A* **1985,** 37, (4), 191-203.
56. Choy, M. M.; Byer, R. L., Accurate second-order susceptibility measurements of visible and infrared nonlinear crystals. *Phys. Rev. B* **1976,** 14, (4), 1693.
57. Graça, M. P. F.; Ferreira da Silva, M. G.; Valente, M. A., Structural and electrical characteristics of $LiNbO_3$ embedded in a 34% SiO_2 glass matrix. *J. Eur. Ceram. Soc.* **2008,** 28, (6), 1197-1203.
58. Fan, C.; Poumellec, B.; Zeng, H.; Lancry, M.; Yang, W.; Bourguignon, B.; Chen, G., Directional writing dependence of birefringence in multicomponent silica-based glasses with ultrashort laser irradiation. *J. Laser Micro Nanoen* **2011,** 6, (2), 158-163.
59. Müller, R.; Zanotto, E. D.; Fokin, V. M., Surface crystallization of silicate glasses: nucleation sites and kinetics. *J Non Cryst Solids* **2000,** 274, (1), 208-231.
60. Cao, J.; Poumellec, B.; Brisset, F.; Helbert, A.-L.; Lancry, M., Angular dependence of the second harmonic generation induced by femtosecond laser irradiation in silica-based glasses: variation with writing speed and pulse energy. *World J. Nano Sci. Eng.* **2015,** 5, 96-106.

61. Wright, S. I.; Nowell, M. M., EBSD image quality mapping. *Microsc. Microanal.* **2006,** 12, (01), 72-84.
62. Desmarchelier, R.; Poumellec, B.; Brisset, F.; Mazerat, S.; Lancry, M., In the heart of femtosecond laser induced nanogratings: from porous nanoplanes to form birefringence. *World J. Nano Sci. Eng.* **2015,** 5, (04), 115.
63. Bricchi, E.; Kazansky, P. G., Extraordinary stability of anisotropic femtosecond direct-written structures embedded in silica glass. *Appl. Phys. Lett.* **2006,** 88, (11), 111119.
64. Bricchi, E.; Klappauf, B. G.; Kazansky, P. G., Form birefringence and negative index change created by femtosecond direct writing in transparent materials. *Opt. Lett.* **2004,** 29, (1), 119-121.
65. Lancry, M.; Brisset, F.; Poumellec, B. In *In the heart of nanogratings made up during femtosecond laser irradiation*, Bragg Gratings, Photosensitivity, and Poling in Glass Waveguides, 2010; Optical Society of America: 2010; p BWC3.
66. Bhardwaj, V.; Simova, E.; Rajeev, P.; Hnatovsky, C.; Taylor, R.; Rayner, D.; Corkum, P., Optically produced arrays of planar nanostructures inside fused silica. *Phys. Rev. Lett.* **2006,** 96, (5), 057404.
67. Zhang, D.-L.; Gao, J.; Hua, P.-R.; Yu, D.-Y.; Pun, E. Y.-B., Appropriate solvent $NaVO_3$ for composition analysis of $LiNbO_3$ crystal using chemical method. *Anal. Chem.* **2013,** 85, (3), 1940-1944.
68. Richter, S.; Heinrich, M.; Döring, S.; Tünnermann, A.; Nolte, S., Formation of femtosecond laser-induced nanogratings at high repetition rates. *Appl. Phys. A* **2011,** 104, (2), 503-507.
69. Lancry, M.; Zimmerman, F.; Desmarchelier, R.; Tian, J.; Brisset, F.; Nolte, S.; Poumellec, B., Nanogratings formation in multicomponent silicate glasses. *Appl. Phys. B* **2016,** 122, (3), 1-8.
70. He, X.; Fan, C.; Poumellec, B.; Liu, Q.; Zeng, H.; Brisset, F.; Chen, G.; Zhao, X.; Lancry, M., Size-controlled oriented crystallization in SiO_2-based glasses by femtosecond laser irradiation. *J. Opt. Soc. Am. B* **2014,** 31, (2), 376-381.
71. Podlipensky, A.; Abdolvand, A.; Seifert, G.; Graener, H., *Femtosecond laser assisted production of dichroitic 3D structures in composite glass containing Ag nanoparticles*. 2005; Vol. 80, p 1647-1652.
72. Fan, C.; Poumellec, B.; Zeng, H.; Desmarchelier, R.; Bourguignon, B.; Chen, G.; Lancry, M., Gold nanoparticles reshaped by ultrafast laser irradiation inside a silica-based glass, studied through optical properties. *J. Phys. Chem. C* **2012,** 116, (4), 2647-2655.
73. Shimotsuma, Y.; Kazansky, P. G.; Qiu, J.; Hirao, K., Self-organized nanogratings in glass irradiated by ultrashort light pulses. *Phys. Rev. Lett.* **2003,** 91, (24), 247405.
74. Jacobs, K., Crystal growth: A tutorial approach. W. Bardsley, D. T. J. Hurle, J. B. Mullin (eds). Proceedings of the Third International School on Crystal Growth, 1977. North-Holland Publishing Company, Amsterdam and New York 1979 IX, 408 Seiten, 237 Abbildungen. *Kristall und Technik* **1980,** 15, (10), 1130-1130.
75. Eaton, S.; Zhang, H.; Herman, P.; Yoshino, F.; Shah, L.; Bovatsek, J.; Arai, A., Heat accumulation effects in femtosecond laser-written waveguides with variable repetition rate. *Opt. Express* **2005,** 13, (12), 4708-4716.
76. Vogel, A.; Noack, J.; Hüttman, G.; Paltauf, G., Mechanisms of femtosecond laser nanosurgery of cells and tissues. *Appl. Phys. B* **2005,** 81, (8), 1015-1047.

77. Miyamoto, I.; Horn, A.; Gottmann, J.; Wortmann, D.; Yoshino, F., Fusion welding of glass using femtosecond laser pulses with high-repetition rates. *J. Laser Micro Nanoen* **2007,** 2, (1), 57-63.
78. Miyamoto, I.; Horn, A.; Gottmann, J., Local melting of glass material and its application to direct fusion welding by ps-laser pulses. *J. Laser Micro Nanoen* **2007,** 2, (1), 7-14.
79. Fokin, V. M.; Nascimento, M. L. F.; Zanotto, E. D., Correlation between maximum crystal growth rate and glass transition temperature of silicate glasses. *J. Non-Cryst. Solids* **2005,** 351, (10), 789-794.
80. Cormier, L., Nucleation in glasses-new experimental findings and recent theories. *Procedia Mater. Sci.* **2014,** 7, 60-71.
81. Stone, A.; Sakakura, M.; Shimotsuma, Y.; Miura, K.; Hirao, K.; Dierolf, V.; Jain, H., Femtosecond laser-writing of 3D crystal architecture in glass: Growth dynamics and morphological control. *Mater. Des.* **2018,** 146.

TABLE OF CONTENTS/ABSTRACT GRAPHIC



KEYWORDS: laser materials processing, second harmonic generation, birefringence, nanograting, textured nanocrystal; glass ceramics.